

TeraShake2: Spontaneous Rupture Simulations of M_w 7.7 Earthquakes on the Southern San Andreas Fault

by K. B. Olsen, S. M. Day, J. B. Minster, Y. Cui, A. Chourasia,
D. Okaya, P. Maechling, and T. Jordan

Abstract Previous numerical simulations (TeraShake1) of large (M_w 7.7) southern San Andreas fault earthquakes predicted localized areas of strong amplification in the Los Angeles area associated with directivity and wave-guide effects from northwestward-propagating rupture scenarios. The TeraShake1 source was derived from inversions of the 2002 M_w 7.9 Denali, Alaska, earthquake. That source was relatively smooth in its slip distribution and rupture characteristics, owing both to resolution limits of the inversions and simplifications imposed by the kinematic parameterization. New simulations (TeraShake2), with a more complex source derived from spontaneous rupture modeling with small-scale stress-drop heterogeneity, predict a similar spatial pattern of peak ground velocity (PGV), but with the PGV extremes decreased by factors of 2–3 relative to TeraShake1. The TeraShake2 source excites a less coherent wave field, with reduced along-strike directivity accompanied by streaks of elevated ground motion extending away from the fault trace. The source complexity entails abrupt changes in the direction and speed of rupture correlated to changes in slip-velocity amplitude and waveform, features that might prove challenging to capture in a purely kinematic parameterization. Despite the reduced PGV extremes, northwest-rupturing TeraShake2 simulations still predict entrainment by basin structure of a strong directivity pulse, with PGVs in Los Angeles and San Gabriel basins that are much higher than predicted by empirical methods. Significant areas of those basins have predicted PGV above the 2% probability of exceedance (POE) level relative to current attenuation relationships (even when the latter includes a site term to account for local sediment depth), and wave-guide focusing produces localized areas with PGV at roughly 0.1%–0.2% POE (about a factor of 4.5 above the median). In contrast, at rock sites in the 0–100-km distance range, the median TeraShake2 PGVs are in very close agreement with the median empirical prediction, and extremes nowhere reach the 2% POE level. The rock-site agreement lends credibility to some of our source-modeling assumptions, including overall stress-drop level and the manner in which we assigned dynamic parameters to represent the mechanical weakness of near-surface material. Future efforts should focus on validating and refining these findings, assessing their probabilities of occurrence relative to alternative rupture scenarios for the southern San Andreas fault, and incorporating them into seismic hazard estimation for southern California.

Online Material: Movies of rupture propagation and simulated wave fields.

Introduction

The two segments of the San Andreas fault south of the 1857 rupture, the San Bernardino Mountains segment and the Coachella Valley segment, have not produced major earthquakes since 1812 and about 1690 (Weldon *et al.*, 2004), respectively. For these two segments, the average recurrence intervals for large events (M_w 7.5 or larger) with

surface rupture are $146 + 91 - 60$ yr and 220 ± 13 yr, respectively (Working Group on California Earthquake Probabilities, 1995). To estimate the expected ground motions in southern California for such events, Olsen *et al.* (2006) simulated 4 min of 0–0.5-Hz wave propagation for M 7.7 earthquake scenarios between Cajon Creek and Bombay Beach

(see Figs. 1 and 2). As the rupture direction for a future event on the San Andreas fault is unknown, simulations with rupture directions toward both northwest and southeast were carried out. These simulations showed strong directivity effects, producing larger ground motions in the rupture direction than in other directions, a qualitative behavior that was expected on the basis of previous studies (e.g., Olsen *et al.*, 1995; Graves, 1998). However, the resulting magnitude and spatial pattern of the directional effects were not expected. In particular, the simulations for scenarios with rupture toward the northwest generated localized areas of strong amplification in Los Angeles, attributed to the line of sedimentary basins (San Bernardino–Chino–San Gabriel–Los Angeles basins) from the northwestern end of the rupture to downtown Los Angeles (see Olsen *et al.*, 2006, fig. 2). This chain of basins forms a low-velocity sedimentary channel that acts as a wave guide, trapping seismic energy and channeling it into the Los Angeles region, particularly for southeast–northwest ruptures. The peak ground velocities (PGV) in localized areas of the Los Angeles area were much larger than

the expected levels for earthquakes of such magnitude (e.g., as obtained from current empirical attenuation relations), most notably in the Whittier–Narrows region (see Olsen *et al.*, 2006, figs. 3 and 4).

The scenario simulations by Olsen *et al.* (2006) (hereafter referred to as TeraShake1) used the kinematic inversion results of the 2002 M_w 7.9 Denali, Alaska, earthquake (Oglesby *et al.*, 2004), representing the source slip-rate function as a sum of six pulses, each of constant shape and propagation velocity, but with successive 1-sec time delays and spatially varying amplitude (independently specified for each pulse). Following Oglesby *et al.*, we took each pulse to be of the form $s(t) = t \exp(-t/[\tau/4])$, where τ defines its effective duration, taken to be 2 sec. The spatially varying amplitudes also were taken directly from Oglesby *et al.*, but using only a 200-km-long and 15-km-wide segment of the Denali slip model (to fit the San Andreas scenario) and with a factor of 4/3 increase of slip to match the target moment magnitude of 7.7. This source model has a maximum and mean slip of 9.9 and 4.6 m, respectively, and a maximum slip rate of

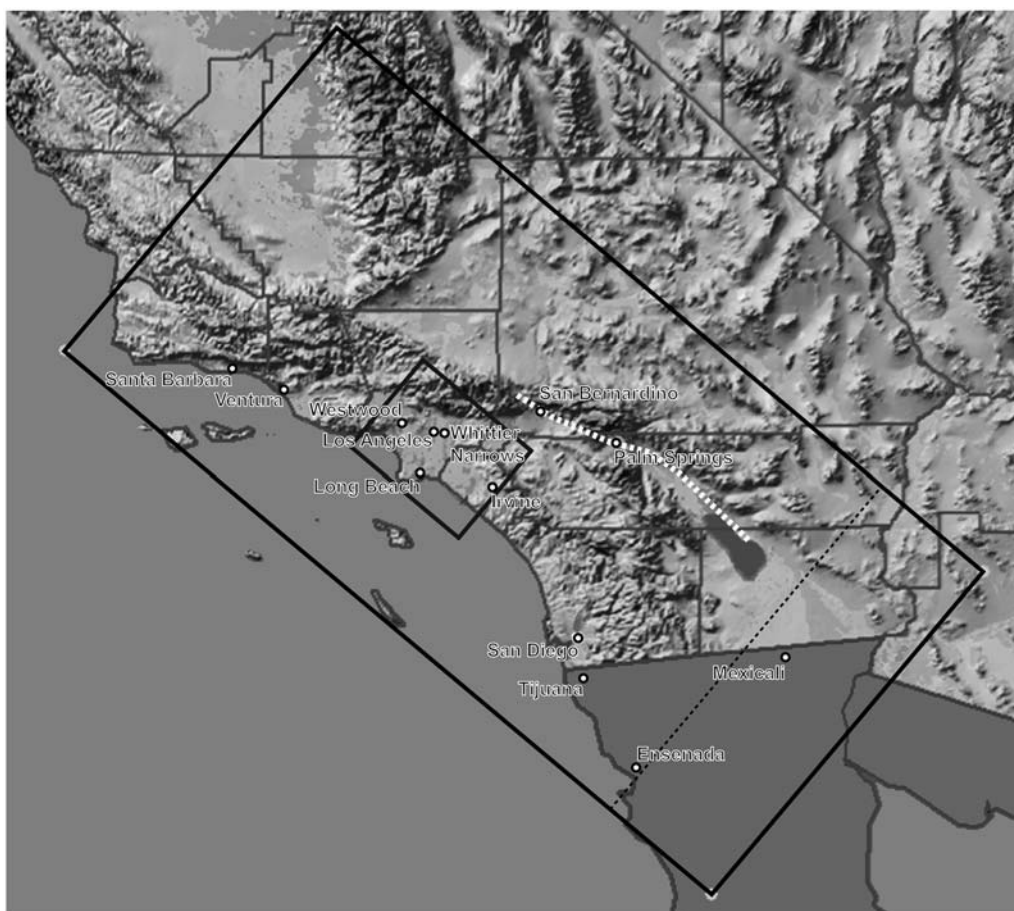


Figure 1. Location map for the TeraShake2 simulations. The large rectangle (121° W, 34.5° N; 118.9511292° W, 36.621696 ; 116.032285° W, 31.082920° N; and 113.943965° W, 33.122341° N) depicts the simulation area, rotated 40° clockwise from north. The small rectangle depicts a section in the Los Angeles area used for peak ground-motion display in Figure 12. The white dotted line depicts the part of the San Andreas fault that ruptured in the TeraShake2 simulations. The $N40^\circ E$ dashed line depicts the location of the cross section used to approximate the crustal structure 50 km along $N130^\circ E$ until the southeastern border of the model. The Cartesian grid for the TS simulations was obtained by mapping the rectangle to Universal Transverse Mercator coordinates

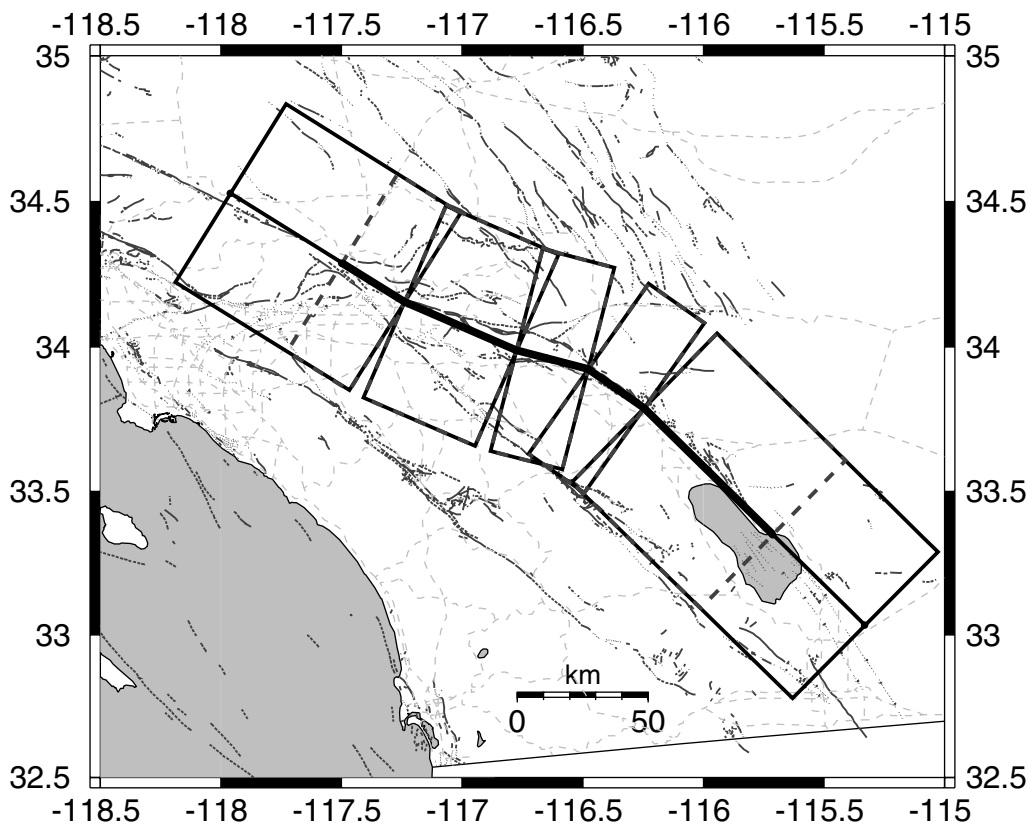


Figure 2. Illustration of the mapping technique used to construct the crustal model from the SCEC CVM3.0 approximating the southern San Andreas fault as a single vertical segment. The thick solid line is the five-segment trace of the southern San Andreas fault used in the USGS 2002 hazard maps. For each of the five segments, a hexahedron (depicted by dashed rectangles) was generated with one horizontal side parallel to and length equal to the segment, the other horizontal edge 80-km long and centered by the segment, and the vertical edge extending from the surface to a depth of 40 km. The southeastern and northwesternmost hexahedra extended 50 km beyond the end points of the fault trace for numerical reasons (solid rectangles). Finally, the hexahedra were merged by rotating the adjacent volumes by an amount that aligned the five segments of the fault into a single vertical planar fault surface. Other fault traces (dark gray lines) and major roads (light gray lines) are also depicted.

4.0 m/sec. The uniform rupture velocity of 3.3 km/sec is on average 87% of the S -wave velocity (from the Southern California Earthquake Center [SCEC] Community Velocity Model [CVM] V3.0), varying from 70% in the deepest parts to 660% in the near-surface low-velocity layers (where the imposed minimum V_s is 500 m/sec). Oglesby *et al.* showed that their source model produces 0.01–0.5-Hz synthetic seismograms in good agreement with the very limited strong-motion data for that earthquake (Oglesby *et al.*, 2004), seemingly making it a reasonable candidate to represent a San Andreas fault event of similar size and style of faulting.

However, it is possible that the unexpectedly large ground motions obtained for the southeast–northwest TeraShake1 simulations are in part attributable to the absence of a realistic level of complexity in the Denali source. One factor that would limit its source complexity is the limited resolution of the inversion: the constraints for the Denali source inversion consisted mainly of teleseismic data with very limited near-source strong-motion data available. A second factor is the parameterization of the source in terms of kinematic parameters, which may impose nonphysical limitations on

the nature of spatial variations of rupture velocity and rupture direction and may fail to conform to physical constraints relating these rupture parameters to variations in the slip-rate amplitude and waveform.

Here we assess the extent to which the level and pattern of ground motion from TeraShake1 are related to the absence of realistic complexity in the Denali source model. To do so, we carry out a series of simulations (hereafter referred to as TeraShake2 or TS2) using the same seismic velocity model and fault geometry as TeraShake1, but with sources derived from spontaneous rupture models that incorporate stress-drop heterogeneity on a scale consistent with inferences from models of the 1992 Landers earthquake.

Basin Model, Earthquake Scenarios, and Numerical Method

In this section, we review the details of the basin model, earthquake scenarios, and numerical method used for the TeraShake1 and TeraShake2 simulations. To facilitate comparison of the ground motions, the wave propagation models

for TeraShake1 and TeraShake2 were chosen to be identical, including the 3D velocity model, fault geometry, and grid intervals in time and space. Furthermore, we adjusted the initial stress state for the dynamic simulations to obtain a predominantly subshear average rupture velocity, resulting in average rupture velocities (3.4 km/sec for TS2.1, 3.3 km/sec for TS2.2, and 2.9 km/sec for TS2.3) that are close to the uniform value of 3.3 km/sec used in TeraShake1 (even though the ruptures are very different in detail, with important consequences that we will discuss).

The areal extent of the TeraShake1 and TeraShake2 ground-motion simulations was a rectangular region, 600 km along N50°W and 300 km along N40°E (see Fig. 1), extending from the surface to a depth of 80 km. The simulations used a $3000 \times 1500 \times 400$ mesh, or 1.8 billion cubes with dimensions 200 m. The 3D crustal structure (Fig. 3) was a subset of the SCEC CVM (Magistrale *et al.*, 2000) version 3.0, with elastic parameters constrained by gravity and reflection seismic data, oil-company drillholes, and shallow geotechnical borings. The near-surface S -wave velocity was truncated at 500 m/sec, allowing the resolution of ground motions up to 0.5 Hz. Surface topography was not included in the simulations. The wave propagation parameters are summarized in Table 1.

The San Andreas fault geometry was modeled by five vertical planar segments from the 2002 U.S. Geological Survey (USGS) National Hazard Maps (Frankel *et al.*, 2002) (Fig. 1). The length and width of the rupture zone were

200 and 16 km, respectively. The TeraShake1 and TeraShake2 ground-motion simulations and TeraShake2 dynamic rupture models were carried out using a fourth-order staggered-grid velocity stress finite-difference code (Olsen, 1994) with a coarse-grained implementation of the memory variables for a constant- Q solid (Day and Bradley, 2001) and Q relations validated against data (Olsen *et al.*, 2003). Both sets of simulations used the FS2 free-surface boundary condition by Gottschämer and Olsen (2001) and the efficient perfectly matched layers (PML) absorbing boundary conditions on the sides and bottom (Marcinkovich and Olsen, 2003). We used a linear slip-weakening friction law in our spontaneous rupture models.

Our dynamic rupture modeling is currently limited to planar fault surfaces aligned with Cartesian coordinate planes normal to the free surface (vertical fault planes). While finite-element methods and some finite-difference methods (e.g., Ely *et al.*, 2006; Cruz-Atienza *et al.*, 2007) can model spontaneous rupture on faults of arbitrary orientation, the more general finite-difference methods are more computationally intensive for the current problem, and additional challenges arise in scaling to the very large problem size considered here. Because of these considerations, we used a two-step approximate procedure to compute the ground motions from the segmented San Andreas fault rupture. Step 1 was a spontaneous rupture simulation for a simplified planar fault geometry. Step 2 was a separate kinematic simulation, using as a source the space-time history of fault

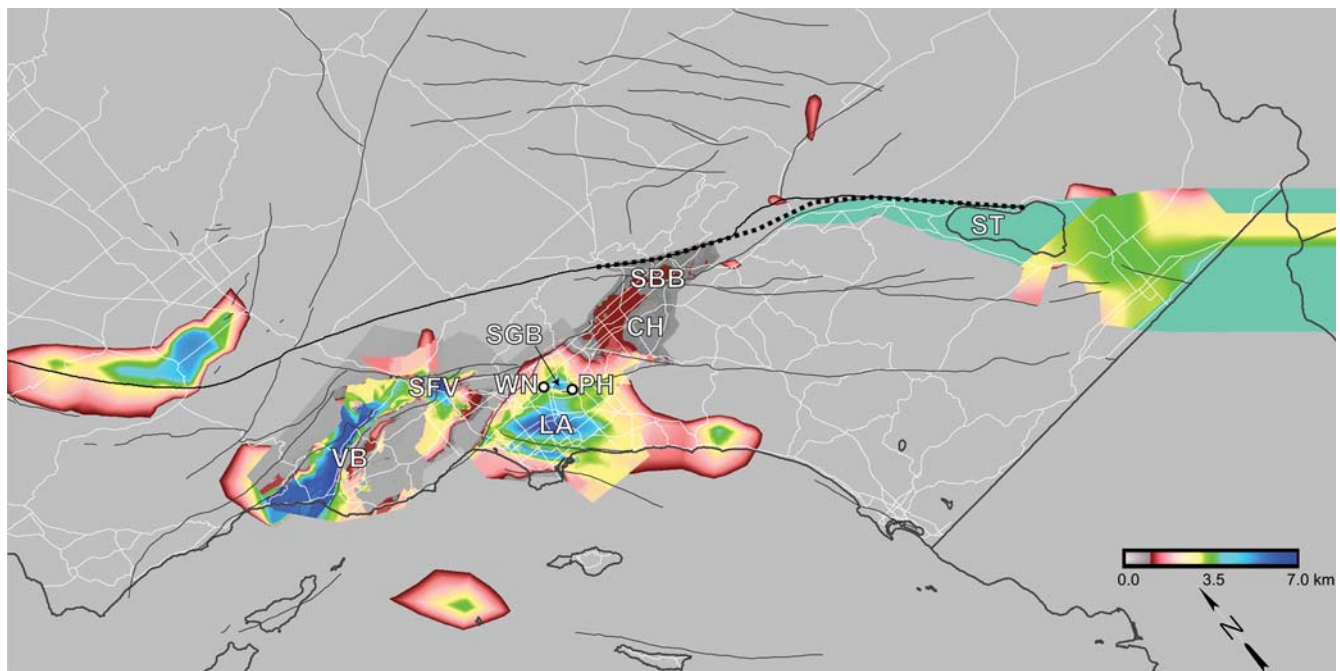


Figure 3. Image of the isosurface for an S -wave velocity of 2.5 km/sec within the TeraShake domain (see Fig. 1), rotated 40° clockwise from north. The dotted line depicts the part of the San Andreas fault that ruptured in the TeraShake2 simulations. Other fault traces (thin black lines), the coastline and state boundaries (thick black lines), as well as major roads (white) are also depicted. CH, Chino basin; LA, Los Angeles basin; PH, Puente Hills; SBB, San Bernardino basin; SFV, San Fernando Valley; SGB, San Gabriel basin; ST, Salton Trough; VB, Ventura basin; and WN, Whittier-Narrows.

Table 1
Wave Propagation Parameters

Parameter	Value
Spatial discretization (km)	0.2
Temporal discretization (sec)	0.011
Lowest P -wave velocity (km/sec)	0.936
Lowest S -wave velocity (km/sec)	0.5
Lowest density (kg/m ³)	1700
Number of timesteps	22,728
Simulation time (sec)	250
Q_s/V_s (V_s in km/sec), $V_s < 1.5$ km/sec	20
Q_s/V_s (V_s in km/sec), $V_s \geq 1.5$ km/sec	100
Q_p	1.5 Q_s

slip from step 1, mapping the latter onto the five-segment San Andreas fault geometry. For step 1, we constructed a 3D velocity model by a mapping procedure, generating a single vertical planar fault surface (see Fig. 2) in the SCEC CVM3.0. For each fault segment, a hexahedron was generated with one horizontal side parallel to and as long as the segment, another side 80-km long, perpendicular to and centered by the segment, and one side extending from the surface to a depth of 40 km. Finally, the hexahedra were merged by rotating the adjacent volumes to generate a 3D model containing a single vertical planar fault surface. This procedure discards the normal stress interaction at fault segment intersections, but these approximations are assumed to be minor in relation to our objectives in this study. A relatively small amount of averaging of the 3D velocity structure was required at the intersection of the subvolumes surrounding each of the five fault segments. Thus, the spontaneous rupture simulations of step 1, while missing the dynamic effects of nonplanar fault geometry, closely match the along-fault wavespeed and density structure of the CVM3.0 model. Then, for step 2, we used the CVM3.0 model, and the original five-segment San Andreas fault model, without the mapping previously described. Thus, when we mapped the slip function determined in step 1 onto the segmented fault model of step 2, we retained compatibility of near-fault material properties for the wave propagation obtained for TeraShake1 and TeraShake2. The slip-rate functions saved on the planar fault from step 1 were inserted on the segmented fault in step 2 by adding $-M_{ij}(x, z, t)/V$ to $S_{ij}(x, z, t)$, where $M_{ij}(t)$ is the ij th component of the moment tensor for the earthquake, V is the cell volume, and $S_{ij}(t)$ is the ij th component of the stress tensor on the fault at time t . Thus, this method for kinematically inserting the source is valid for arbitrary orientation of the subfaults.

Modeling of the Source

Dynamic Source Description

In our dynamic rupture modeling, we assume that the frictional strength τ is proportional to the normal stress σ_n , with the convention that negative normal stress corresponds to compression

$$\tau = -\mu_d(l)\sigma_n, \quad (1)$$

where the coefficient of friction $\mu_d(l)$ was defined using a simple linear slip-weakening friction law, with

$$\begin{aligned} \mu_d(l) &= \mu_s - (\mu_s - \mu_d)l/d_c, & l < d_c; \\ \mu_d(l) &= \mu_d, & l \geq d_c, \end{aligned} \quad (2)$$

where l is the (scalar) slip, μ_s and μ_d are the coefficients of static and dynamic friction, respectively, and d_c is the critical slip-weakening distance. In our study, we arbitrarily used $\mu_s = 1$ and $\mu_d = 0$ for all dynamic rupture models, that is, assumed a complete static stress drop. The friction law was implemented in our fourth-order staggered-grid finite-difference method using the stress-glut method (Andrews, 1999). Despite the choice of dynamic friction level, little or no backslip was generated using the stress-glut method. Rupture was nucleated artificially by elevating the shear stress 1.2% above the local normal stress in a circular patch of radius 3 km near the end of the fault. The slip direction was limited to that of the initial shear stress, that is, in the long direction of the fault (rake angle 180°), and rake rotation was not allowed. A relatively coarsely meshed version of the seismic velocity model (with a grid spacing of 200 m) was used in exploratory simulations to estimate a distribution of stress and friction parameters that allowed rupture propagation with an overall subshear rupture velocity. We sought a predominantly subshear rupture model to provide a more direct comparison with the subshear model used in TeraShake1 (Olsen *et al.*, 2006), in recognition that average rupture velocities inferred in source inversions are commonly subshear with occasional supershear segments. Then, in order to ensure sufficient accuracy of the rupture propagation, the same parameters were used to simulate dynamic rupture propagation in a higher-resolution model with a grid spacing of 100 m. The modeling parameters for the dynamic rupture simulations are summarized in Table 2.

The initial shear-stress distributions were generated from a sequence of approximations of the Peyrat *et al.* (2001) dynamic inversion results for the M 7.3 1992 Landers earthquake (see Fig. 4a). Specifically, the shear stress was gener-

Table 2
Dynamic Rupture Parameters

Parameter	Value
Spatial discretization (km)	0.1
Temporal discretization (sec)	0.0055
Lowest P -wave velocity (km/sec)	0.936
Lowest S -wave velocity (km/sec)	0.5
Lowest density (kg/m ³)	1700
Number of timesteps	21,818
Simulation time (sec)	120
Q_s/V_s (V_s in km/sec), $V_s < 1.5$ km/sec	20
Q_s/V_s (V_s in km/sec), $V_s \geq 1.5$ km/sec	100
Q_p	1.5 Q_s

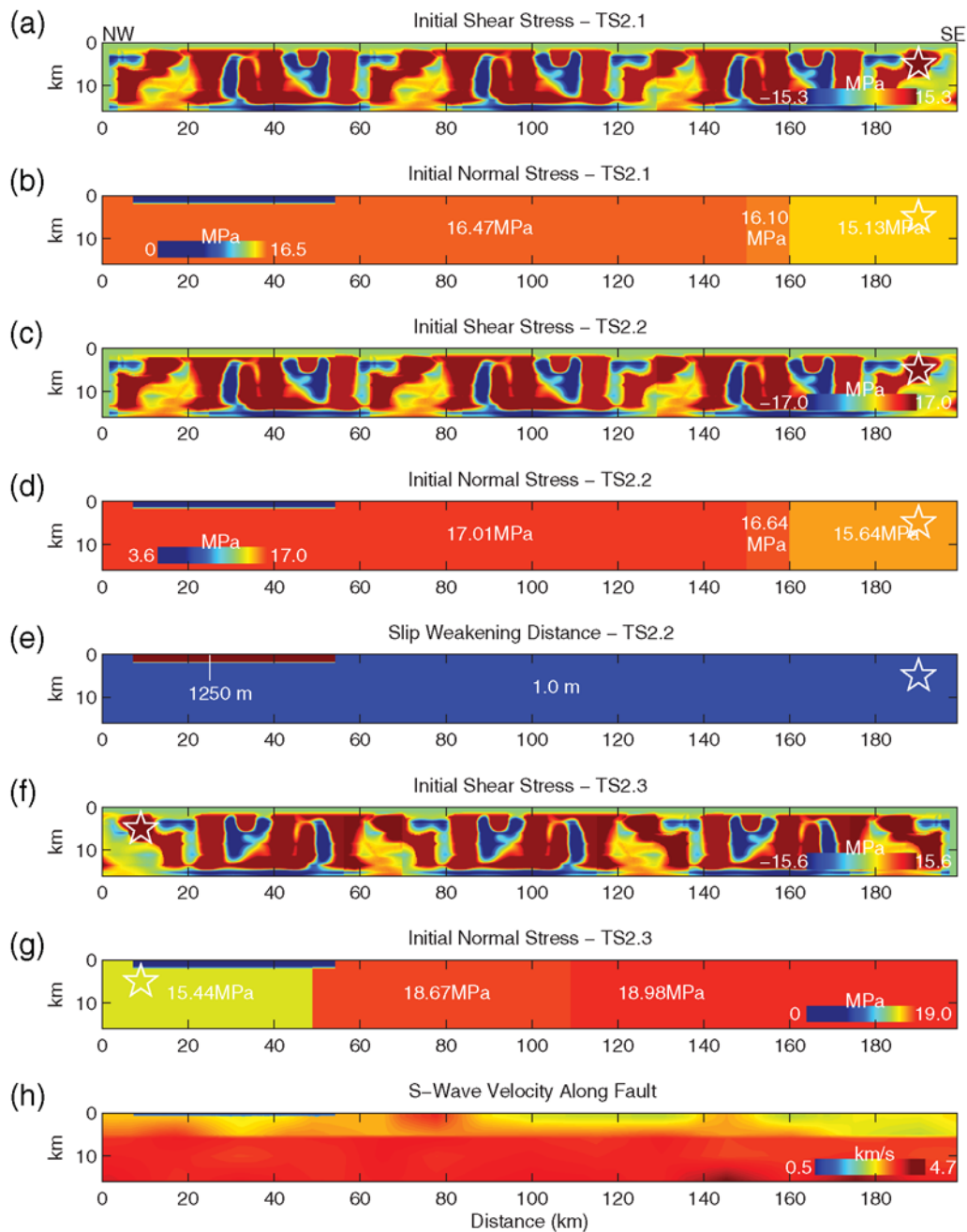


Figure 4. Dynamic rupture parameters for the TeraShake2 simulations. The slip-weakening distance was uniform (1.0 m) for the TS2.1 and TS2.3 scenarios. The white stars depict the rupture nucleation areas.

ated by repeating the southeasternmost 60 km of the Peyrat *et al.* solution three times followed by the southeasternmost 20 km of the Peyrat *et al.* solution. The synthetics obtained by Peyrat *et al.* provided a good fit to near-field long-period (<0.5 Hz) strong-motion data from the Landers event, which occurred on a near-vertical fault with a right-lateral focal mechanism, similar to the expected characteristics of a large earthquake on the southern San Andreas fault. Thus, the complexity of the dynamic source descriptions developed here has some observational basis in seismic records in the

same frequency band (0–0.5 Hz) that is targeted in the current study.

Three different high-resolution ($dx = 100$ m) dynamic rupture simulations were generated and used as sources for three different TeraShake2 wave propagation runs ($dx = 200$ m) for frequencies up to 0.5 Hz, similar to the TeraShake1 scenarios. The first two, TS2.1 and TS2.2, are nucleated at the southeast end of the fault and rupture southeast to northwest. The third, TS2.3, was nucleated at the northwest end and ruptured northwest to southeast. The

TS2.1–2.3 ruptures were generated by the initial shear-stress fields shown in Figure 4a,c,f, respectively. The distributions of initial normal stress for TS2.1–2.3 are shown in Figure 4b, d,g, respectively. We found that, given the assumed initial shear-stress fields and simplified friction model, a piecewise-constant lateral increase of normal stress in the rupture direction was necessary to constrain the rupture speed to subshear values. However, the specific patterns of normal stress increase that allowed rupture nucleation and an average subshear rupture speed for opposite rupture directions were different due to the spatial variation of the elastic parameters (which are not symmetrically disposed with respect to the San Andreas fault). Although relatively small, the differences between the initial normal stress increase in the rupture direction for TS2.1–2.3 (2%–14%) were critical to ensure initiation and generally subshear rupture propagation. We expect that this lateral trend in normal stress is nonphysical and would likely be eliminated by a more realistic friction law (with a demand for finer numerical resolution), for example, by permitting nucleation under a much wider range of initial stress conditions. Nonetheless, the asymmetry of this result with respect to rupture direction underscores the fact that in a state-of-the-art 3D model, in general, it is not possible to laterally mirror the dynamic rupture parameters and obtain identical rupture propagation, a device oftentimes used for kinematic wave propagation studies.

Besides scaling of the results to generate a common moment magnitude event, the primary modifications to the Peyrat *et al.* (2001) dynamic rupture parameters were done in the near-surface part of the fault. Here, the initial stress fields and slip-weakening distance obtained from the Landers study required special attention, because the inversion used a plane-layered crustal model with a relatively high, lowest S -wave velocity of 1.98 km/sec. In particular, extending the scaled Landers results with d_c equal to 1 m and a maximum static stress drop of 15.3 MPa into the near-surface area of the fault using the SCEC CVM3.0 with S -wave velocities as low as 500 m/sec produced large and nonphysical values of slip and slip rate (as would be expected). The low S -wave velocities were mostly limited to the intersection of the fault with the San Bernardino area (7.5–54.5 km from the northwestern end of the fault, see Fig. 4h). This result is consistent with the expectation that the shallow stress and friction levels in low-velocity sediments are significantly different from those in the deeper parts of the fault and may also suggest a transition to velocity strengthening friction (e.g., Marone and Scholz, 1988) at shallow depth. While modeling the state of friction in different parts of the crust is an important problem attracting attention in current research (e.g., Ide, 2002; Tinti *et al.*, 2005), it is beyond the scope of our study. Instead, in the upper 2 km, we limited the initial shear stresses and used trial and error to modify the dynamic rupture parameters until average subshear rupture velocities were obtained. For the TS2.1 and TS2.3 rupture simulations, the initial shear stress was set to zero in the uppermost 1 km of the crust, and between 1–2-km depth, the shear stress derived by

Peyrat *et al.* (2001) was multiplied by a linear tapering function with values of 0 and 1 at 1- and 2-km depth, respectively. The reduced stresses resulted in reduced bounds on shallow slip and slip rates. The initial normal stress was modified only in the low-velocity sediments of the San Bernardino area. For TS2.1 and TS2.3, this was done following a procedure similar to that used for the initial shear stress. While this tapering procedure in the near surface prevented undesirable numerical artifacts in slip and slip rate (alternating small and very large values at adjacent grid points), the rupture speed for TS2.1 jumped to supershear values inside the near-surface material of the San Bernardino area. Because supershear rupture propagation has been inferred from both strong-motion data (Archuleta, 1984; Bouchon *et al.*, 2001; Peyrat *et al.*, 2001; Dunham and Archuleta, 2005) and laboratory crack experiments (Xia *et al.*, 2004), TS2.1 was kept as an acceptable rupture model. However, we generated the additional southeast–northwest rupture TS2.2 to produce a scenario with subshear rupture speed throughout the fault. This was obtained by the following modification (in the low-velocity sediments of the San Bernardino area only): (1) linearly tapering the initial normal stress to 20% of its value at 2 km for depths 1.3–2 km and extending the value at 1.3 km to the surface, (2) computing the initial shear stress as 1/3 of the initial normal stress for depths 0–2 km, and (3) defining a very high value of d_c in the upper 1.3 km, linearly increased from the value at 2-km depth (1 m). These modifications generated a near-surface weak layer, that is, a zone of negative dynamic stress drop, as studied experimentally by Brune and Anooshehpour (1998) and numerically by Day and Ely (2002) and Anderson *et al.* (2003), in the San Bernardino region. These modifications generated subshear rupture propagation fault wide for the TS2.2 scenario. Table 3 summarizes the stress and d_c distributions used in the TS2.1–2.3 rupture models.

Kinematic Source Description

Because the TeraShake1 (inferred from the Denali event) and TeraShake2 (inferred from the Landers earthquake) models differ only by their source descriptions, it is imperative to compare the rupture propagation for the two sets of simulations. Figure 5 shows a snapshot of the slip rates on the fault 27.5 sec after rupture initiation for models derived from the Landers (TS2.1) and Denali earthquakes (TS1.3). (See a movie comparing sets of rupture propagation in the electronic version of *BSSA*.) The more complex source from the Landers earthquake is characterized by strong variations in rupture speed as well as frequent separation into several slipping areas of highly varying shape and slip rate. In contrast, the simpler rupture from the Denali earthquake has uniform rupture velocity and slip contained in six consecutive elementary pulses. Note, however, that the two ruptures propagate with the same average rupture speed (approximately 3.3 km/sec), except for the leftmost 25% (the San Bernardino area), where the TS2.1 source jumps

Table 3
Overview of Rupture Models

	TS2.1	TS2.2	TS2.3	TS1
M_w	7.7	7.7	7.7	7.7
Rupture area (km ²)	3200	3200	3200	3200
Rupture direction	southeast–northwest	southeast–northwest	northwest–southeast	southeast–northwest or northwest–southeast
Initial shear stress	Figure 3a	Figure 3c	Figure 3f	N/A
Initial normal stress	Figure 3b	Figure 3d	Figure 3g	N/A
d_c	1.0 m	Figure 3e	1.0 m	N/A
Average stress drop (MPa)	5.2	5.4	5.4	N/A
Maximum slip (m)	9.2	8.2	8.5	9.9
Average slip (m)	4.2	4.2	4.2	4.0
Maximum peak slip rate (m/sec)	4.6	4.8	4.4	4.0
Average peak slip rate (m/sec)	1.7	1.6	1.7	1.3
Average rupture velocity (km/sec)	3.4	3.3	2.9	3.3

to supershear speeds, as previously discussed. Average duration of slip (at a given point) is also similar in the two sets of models, although much more variable in the latter.

Figure 6 shows the final slip and maximum slip rates obtained from the TS2.1–2.3 rupture models, compared to those for the TS1.2–1.3 from the Denali earthquake, and Table 3 lists the average and maximum slip, average rupture speed, and average and maximum peak slip rates. While values of both maximum slip (about 10 m) and maximum slip rates (about 5 m/sec) are similar for the two sets of sources, the spatial patterns of the parameters are very different on the fault. The ruptures derived from the Denali earthquake generate relatively smooth distributions of slip and maximum slip rates, characterized by large (typically 20 km or larger) asperities. In contrast, the slip and slip rates from the source inferred from the Landers earthquake depict smaller asperities (typically 10 km or less), outlining the areas of high initial shear stress (see Fig. 4a,c,g). Note the strong connectivity of the slipping areas required for the dynamic ruptures to develop into a large earthquake, as pointed out by, among others, Peyrat *et al.* (2001) and Nielsen and

Olsen (2000) for spontaneous rupture models of the 1992 Landers and 1994 Northridge earthquakes, respectively. It is also interesting to note that, while the static stress drop in the near-surface part of the fault was purposely set to zero or very small values, some of the largest slip rates are found on this part of the fault for the dynamic models. These localized areas of large slip rates are generally located immediately above the large asperities (see Fig. 6c–h) and are likely a combined amplification effect from the underlying stress concentration, the proximity of the free surface, and the lower rigidity of the shallow part of the model. Finally, the supershear speeds obtained in the San Bernardino area for the TS2.1 model caused remarkable increases in near-surface slip (up to 20%) and maximum slip rates (up to 50%) as compared to the subshear rupture models (TS2.2–2.3) in this area.

Ground-Motion Modeling

In step 2, the slip rates obtained from the three spontaneous rupture sources previously described (TS2.1–2.3)

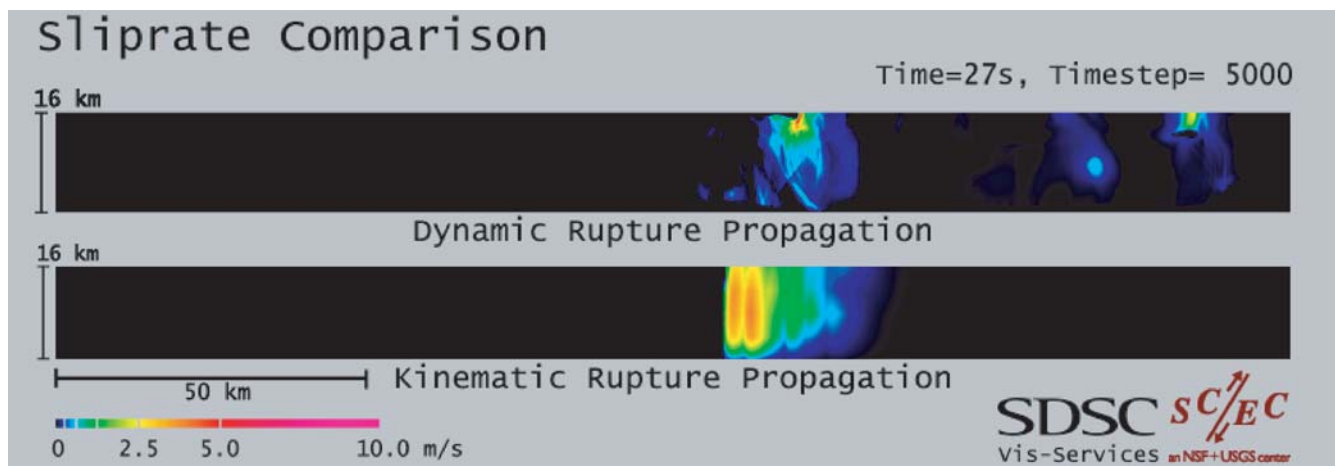


Figure 5. Comparison of snapshots of slip rate for dynamic (top, TeraShake 2.1) and kinematic (bottom, TeraShake 1.3) rupture derived from the Denali earthquake propagation 27.5 sec after initiation.

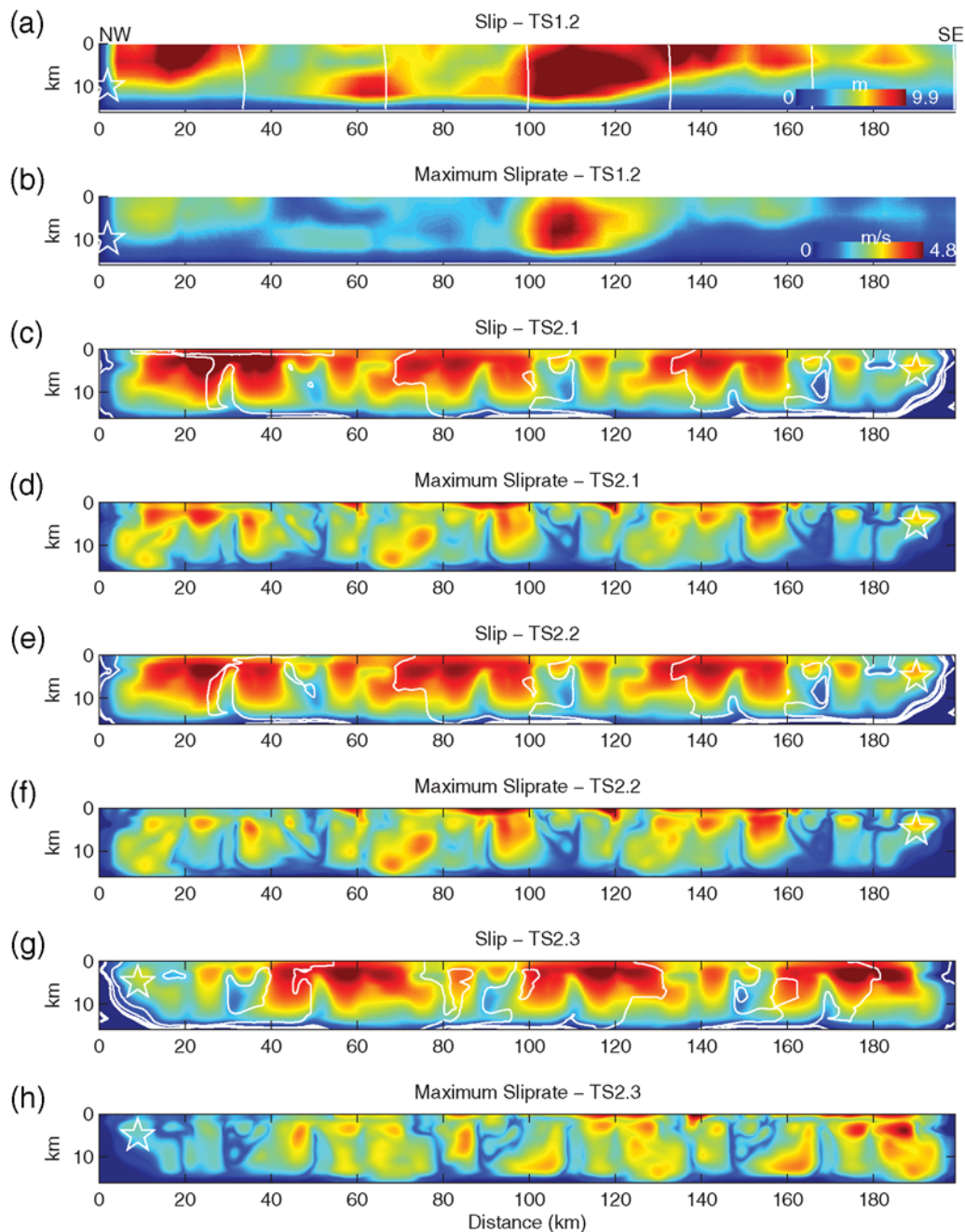


Figure 6. Kinematic rupture parameters (slip and maximum slip rate) for the TeraShake1 and TeraShake2 simulations. The white contours depict the rupture time from 10 to 70 sec with 10 sec interval.

were then low-pass filtered at 0.5 Hz and inserted as a kinematic source at 200-m spacing onto the 200-km long, five-segment (vertical) approximation of the southernmost San Andreas fault, as was the case in the TeraShake1 simulations. Wave propagation was simulated for 4 min inside the 600×300 -km model area shown in Figure 1, with a depth extent of 80 km.

The ground-motion patterns obtained from the sources derived from the Landers and Denali earthquakes show notable similarities and differences, related to the rupture pat-

terns previously discussed. Figure 7 shows distributions of peak ground velocity (PGV) for the three TeraShake2 ruptures (TS2.1–2.3). (See movies of the cumulative PGVs in the electronic version of *BSSA*.) The PGV patterns from the TeraShake2 source descriptions contain the same overall features as for the TeraShake1 results reported by Olsen *et al.* (2006), such as rupture directivity and localized amplification near Whittier–Narrows (see Figs. 1 and 3 for location) due to a wave guide located along the northern edge of the San Bernardino–Chino–San Gabriel–Los Angeles basins.

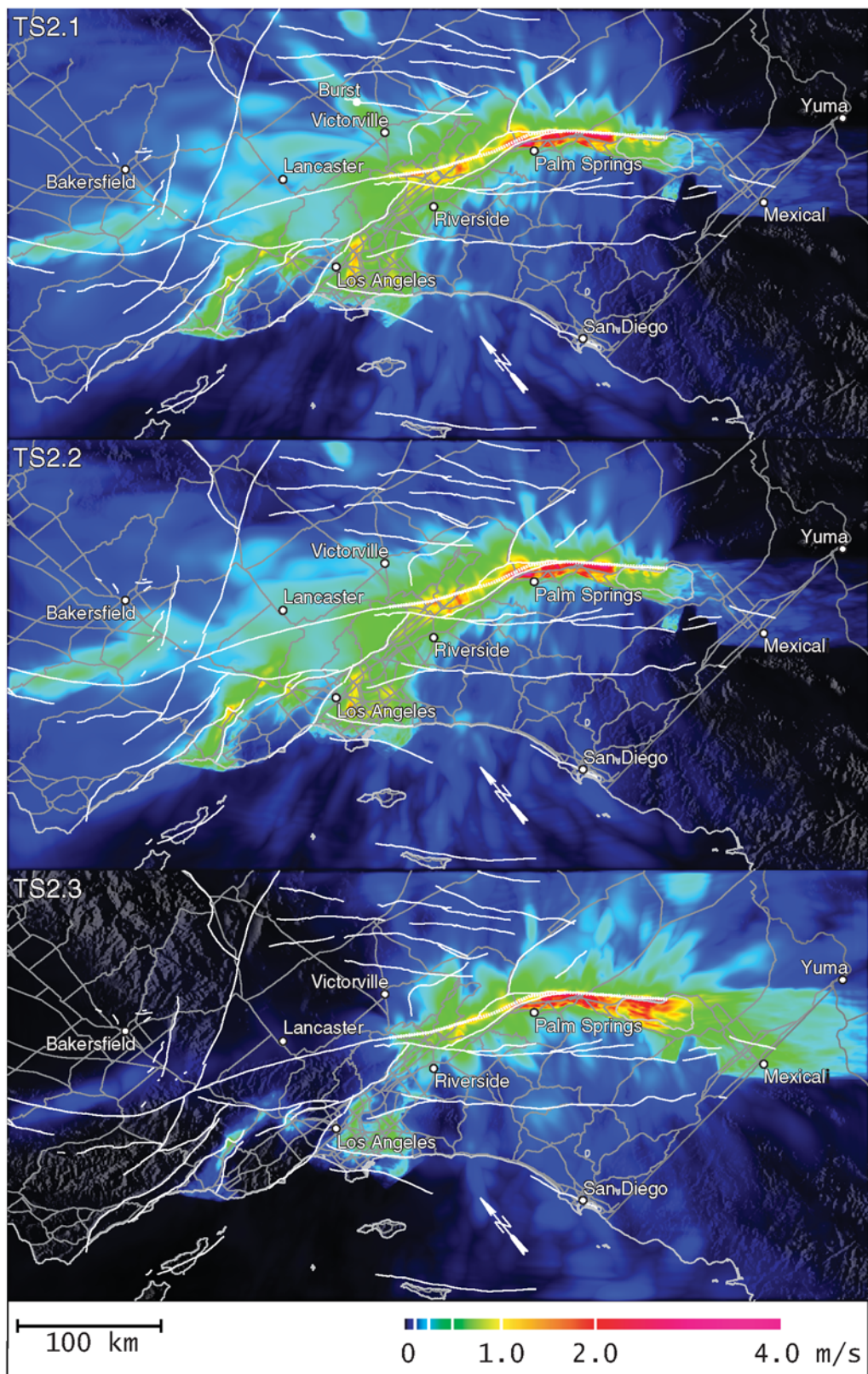


Figure 7. PGVs for the TeraShake2 simulations. White lines depict fault traces and county lines. The dotted line depicts the part of the San Andreas fault that ruptured in the TeraShake2 simulations.

However, the path of the waves propagating westward from the San Bernardino area toward the Los Angeles basin shows an additional complication. The Love waves are wrapped around the Puente Hills (see Fig. 3 for location), channeling seismic energy not just into the Whittier–Narrows area, but also into the southern part of the Los Angeles basin (see snapshots of the instantaneous velocity magnitude for TS2.1 in Fig. 8 and $\text{\textcircled{E}}$ movies of the instantaneous velocity magnitude in the electronic version of *BSSA*). This multipathing effect separates the seismic energy into two branches, with the (northern) wave guide through Whittier–Narrows generating the strongest amplification for the TeraShake2 scenarios (as it did in TeraShake1). The maximum PGVs away from the fault for TS2.1–2.2 were similar (153–154 cm/sec) and were both generated by the northern wave guide, near Whittier–Narrows for TS2.1, and in the Los Angeles basin for TS2.2 (13-km south of the TS2.1 maximum). The PGVs from the southeast–northwest scenarios (TS2.1–2.2) in the Los Angeles basin are about three times larger than those from the northwest–southeast scenario (TS2.3) due to directivity effects (see, e.g., the synthetic seismograms in Figs. 9 and 10 versus Fig. 11, Whittier–Narrows). In turn, southeast of the causative fault, the peak motions for TS2.3 are three to four times larger than those for the southeast–northwest rupture scenarios (see, e.g., Figs. 9 and 10 versus Fig. 11, Mexicali).

While the patterns of PGVs for TeraShake1 and TeraShake2 simulations with rupture in the same direction are similar, the largest PGVs associated with the wave-guide effects and deep basin amplification for the TS2 rupture are generally smaller than those from the source derived from the Denali earthquake by a factor of 2–3 (see Fig. 12). This finding might appear somewhat surprising considering the larger near-surface slip rates for the spontaneous rupture (see Fig. 6). The smaller PGV values for the latter models are mainly caused by less coherent wavefronts generated by the complex dynamic source, as compared to those from the much simpler TeraShake1 rupture propagation. The decreased coherence of the TS2 wavefronts is caused by (1) the smaller length scale of the TS2 (generally 10 km or less) versus TS1 (generally 20 km or larger) asperities in the slip distributions and/or (2) the abrupt changes in direction and speed observed in the spontaneous rupture propagation (TS2) versus the much simpler parameterization of six elementary pulses propagating with constant rupture velocity (3.3 km/sec) for TS1. To estimate the relative contributions of cause 1 and cause 2, we carried out an additional simulation (Landers Kinematic) with the slip distribution of TS2 and the rupture parameterization (path, speed, and shape of the rupture pulse) of TS1. The maximum PGV for Landers Kinematic in the Whittier–Narrows region associated with the wave-guide effects previously discussed is 2.6 m/sec, 70% larger than the value obtained from the TS2 scenarios with southeast–northwest rupture direction and 19%–48% smaller than the values obtained from the TS1 scenarios with southeast–northwest rupture direction. This result, along

with the similarity of the size and shape of the wave-guide-amplified region for Landers Kinematic and the TS1 scenarios (see Fig. 12), demonstrates that the decreased coherence of the TS2 wavefronts is mainly caused by (2), with a minor contribution from (1). However, despite the lower PGVs, the TeraShake2 simulations suggest that a large earthquake on the southern San Andreas fault may still pose a significant seismic hazard for many communities located close to the fault (e.g., Palm Springs, Riverside, and San Bernardino) and sites affected by strong directivity (i.e., Victorville for southeast–northwest ruptures) or basin effects (i.e., downtown Los Angeles, Long Beach, and Whittier–Narrows, particularly for southeast–northwest ruptures). Moreover, the long duration of shaking exceeding 1 min is a concern at many sites, such as in areas with concentrations of high-rise buildings (e.g., downtown Los Angeles, Long Beach, Westwood, and Irvine), which are susceptible to long-period ground motions. The extended durations are primarily a problem at basin locations, while durations at rock sites (e.g., Victorville and Palm Springs) are much shorter. However, a more in-depth discussion of the potential seismic risk to structures from the TS2 scenarios is beyond the scope of our study, and interested readers are referred to the case studies of similar earthquake scenarios by Krishnan *et al.* (2006a, b).

The main differences between the ground motions from TS2.1 and TS2.2 are found along the northwesternmost part of the rupturing fault in the San Bernardino area where, unlike TS2.2, the TS2.1 rupture propagated at supershear velocity. The supershear rupture propagation is seen to increase the PGVs near the fault in San Bernardino by up to a factor of 2 (see Figs. 7 and 13, top). The synthetic seismograms at San Bernardino show the same features of near-fault ground motion from supershear rupture propagation as pointed out by Dunham and Archuleta (2005). These features include an initial large-amplitude phase (arriving at about 55 sec) on both the fault-parallel (FP, approximately east–west, *A*) and fault-normal components (FN, approximately north–south, *B*), and a later phase (62–69 sec, *C/D*) predominantly on the FN component, with a slightly smaller amplitude. The arrival at *A* corresponds to the supershear rupture pulse, while the *C/D* pulse may be a combination of the Rayleigh (*C*) and possible healing phases (*D*) inferred in Dunham and Archuleta (2005). Smaller increases in peak motions from the supershear rupture are also seen further northwest of the rupturing fault, for example, in the Los Angeles and Ventura basins, promoted by a strong directivity of the rupture in these areas for the TS2.1–2 scenarios.

A notable characteristic feature in the TeraShake2 PGV distributions is the star burst pattern of increased peak values radiating out from the fault (see Fig. 7 and Chourasia *et al.*, 2007, fig. 6a). These rays of elevated peak ground motions are generated in areas of the fault where the dynamic rupture pulse changes abruptly in either speed, direction, or shape. For this reason, the bursts of elevated ground motion are also correlated with pockets of large near-surface slip rates on the

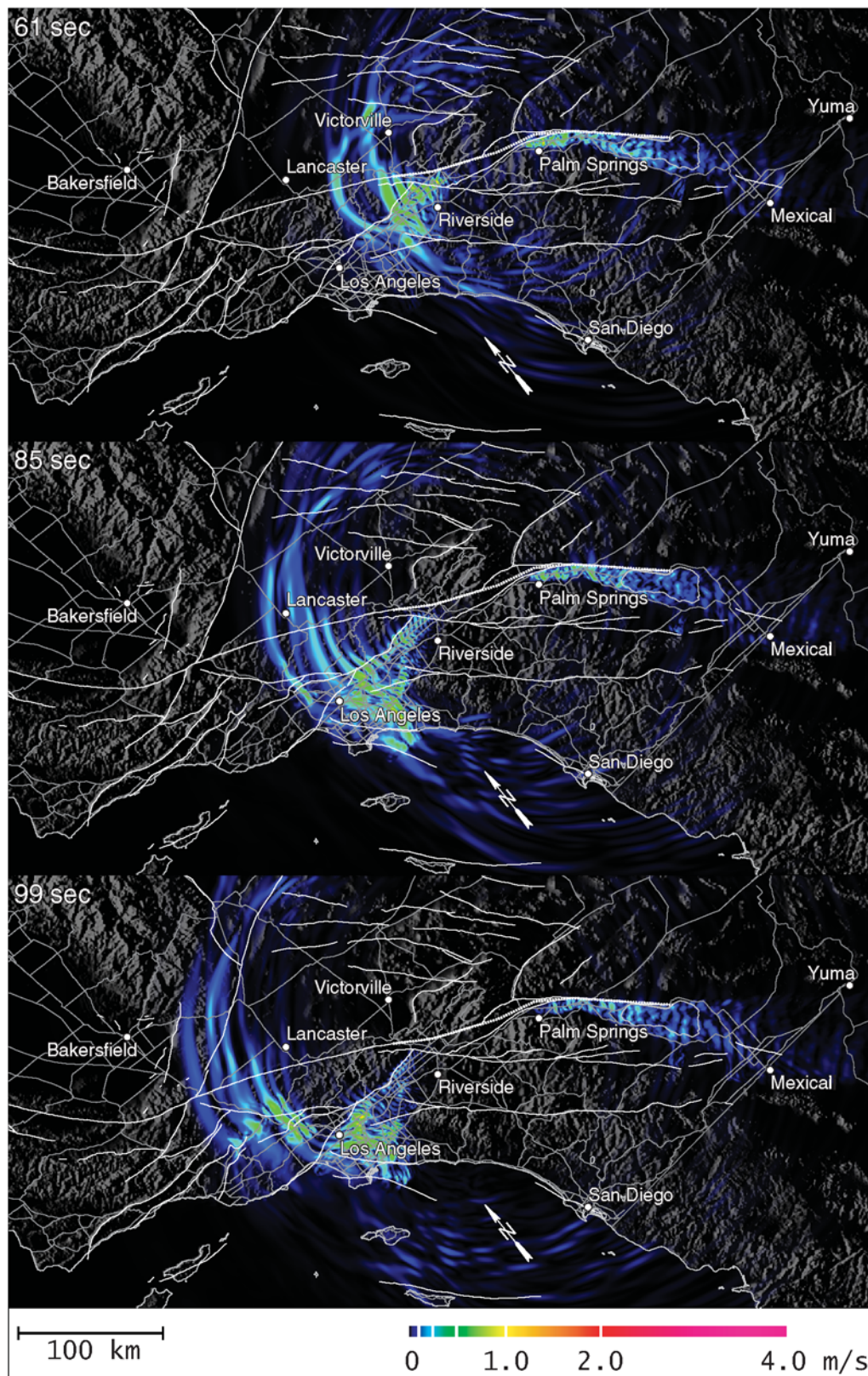


Figure 8. Snapshots of instantaneous PGVs for the TeraShake2.1 simulation. White lines depict fault traces and county lines. The dotted line depicts the part of the San Andreas fault that ruptured in the TeraShake2 simulations. Note the multipathing effect of the eastward propagating waves starting at the Puente Hills (see Fig. 3 for location).

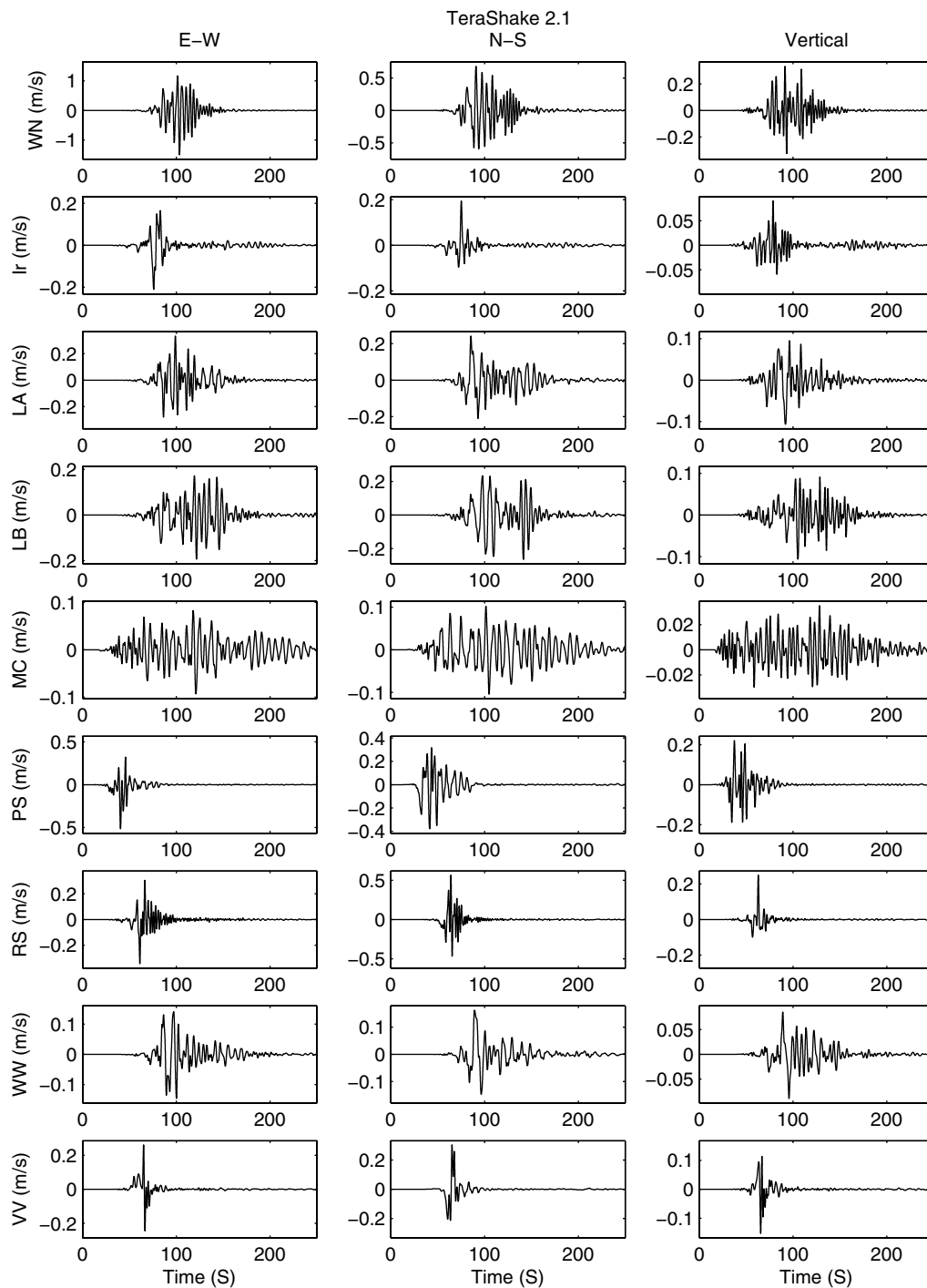


Figure 9. Synthetic seismograms at selected locations (see Fig. 1) in the model area for the TeraShake 2.1 simulation. WN, Whittier-Narrows; Ir, Irvine; LA, downtown Los Angeles; LB, Long Beach; MC, Mexicali; PS, Palm Springs; RS, Riverside; WW, Westwood; and VV, Victorville.

fault (see Fig. 6). Such a pattern is absent from the PGV distributions for the TeraShake1 simulations by Olsen *et al.* (2006), due to the very limited effective variation in rupture speed and constant shape of the source time functions obtained from the kinematic inversion procedure used by Oglesby *et al.* (2004). This enhanced radiation from the

TeraShake2 simulations in directions at high angle to the fault comes at the expense of seismic energy in the main forward-directivity cone, which is one of the principal consequences of the rupture model derived from the Landers earthquake stress-drop distribution, in comparison with the simpler TeraShake1 source models. One of the rays is radiat-

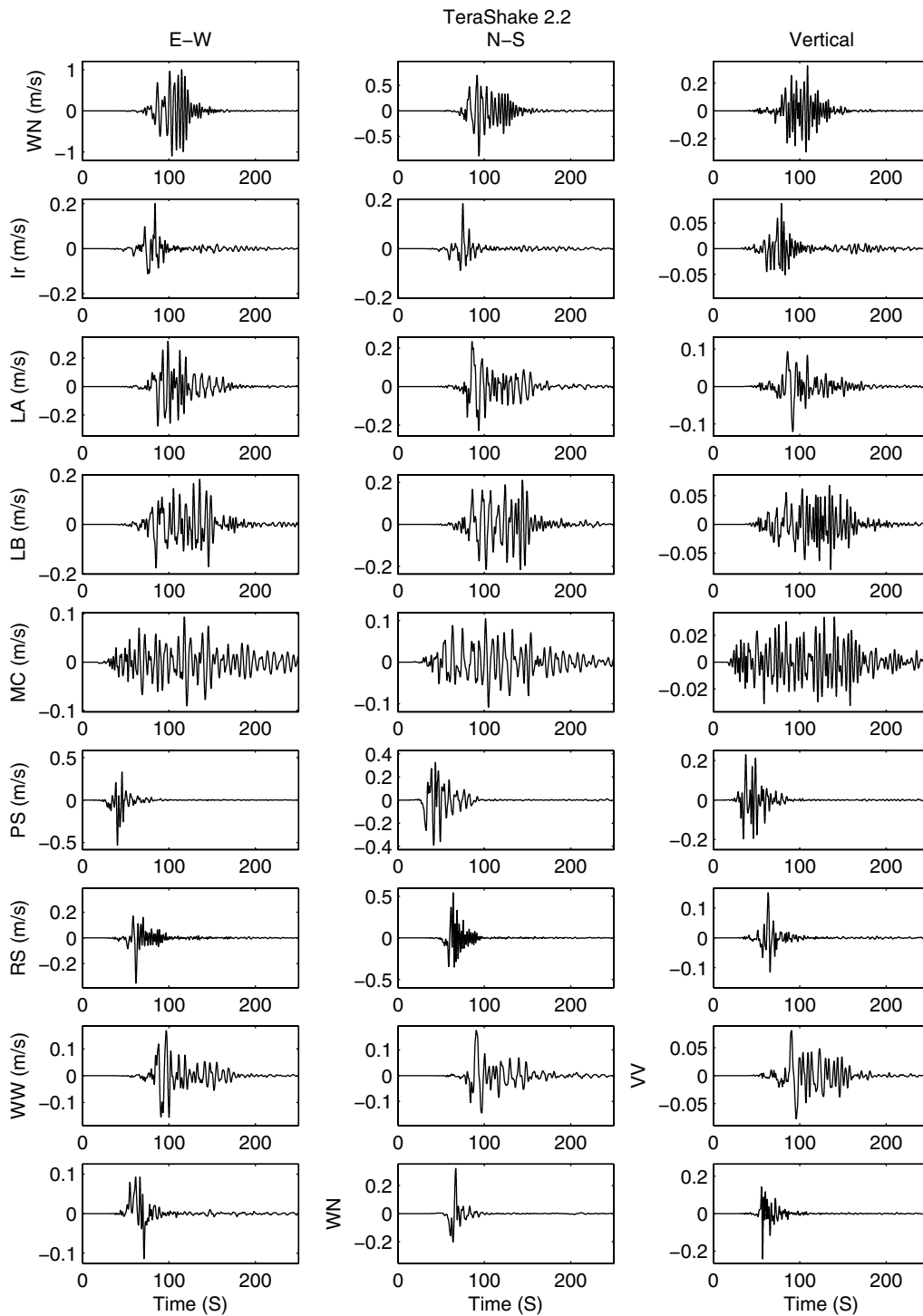


Figure 10. Same as Figure 9, but for TeraShake 2.2.

ing northward from the San Bernardino area, past Victorville. In this case, the phenomenon is connected to the supershear rupture propagation for TS2.1 (and thus absent for TS2.2). Figure 13 (bottom) shows synthetic seismograms at a location inside this particular band of increased amplification. The largest amplitude pulses on the horizontal components propagate with a subshear speed inside the band.

Limitations of the Modeling Results

The principal goal of this study of southern San Andreas fault scenarios was to assess the effects on ground motion of source models with a more realistic level of space-time complexity, relative to the low-resolution source model (derived from the Denali earthquake) used by Olsen *et al.* (2006). We

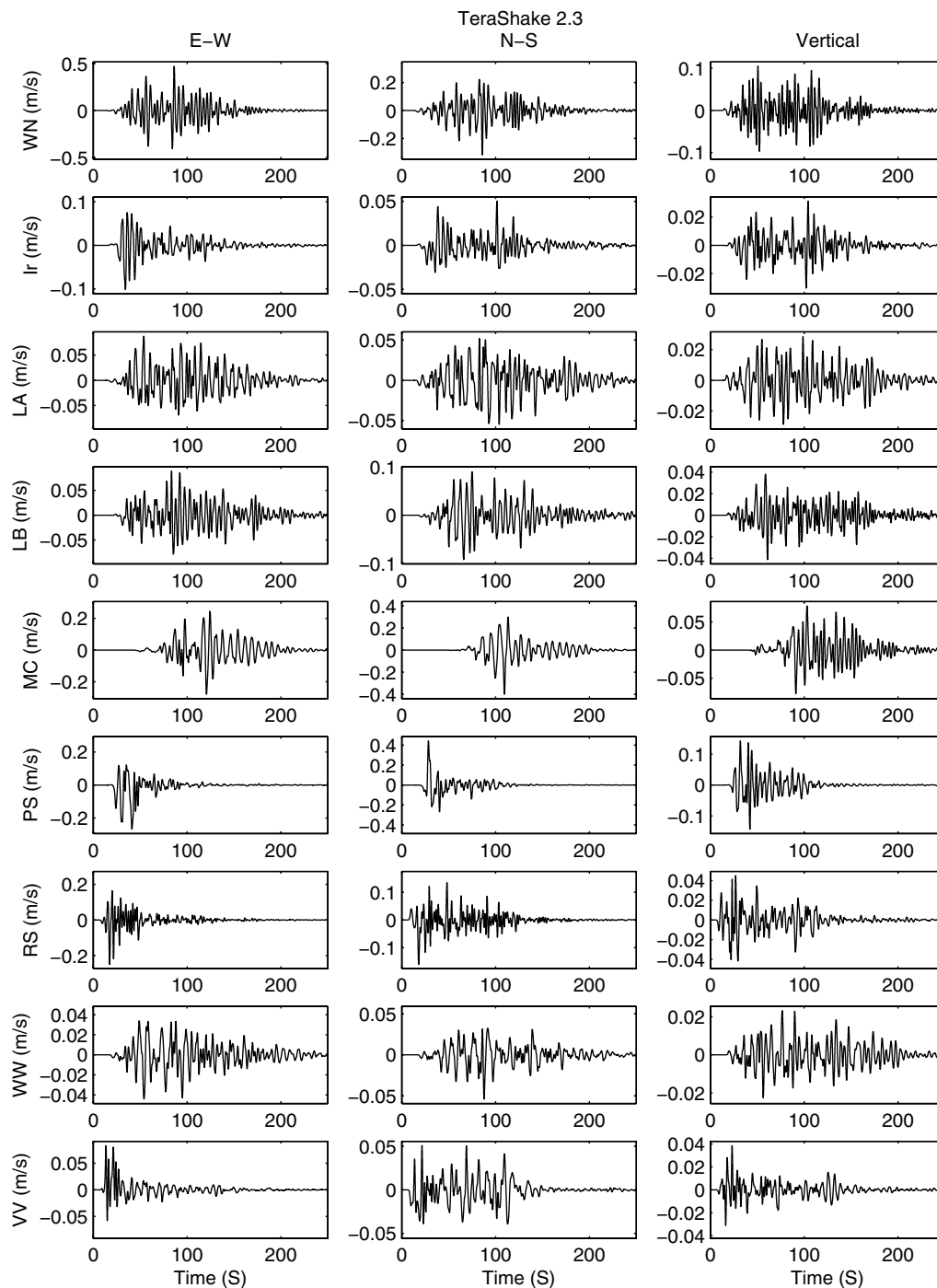


Figure 11. Same as Figure 9, but for TeraShake 2.3

achieved source complexity through enhanced spatial heterogeneity of static stress change (at a level supported by observational studies) and through space-time variability of slip rate (derived from spontaneous rupture modeling). In this section, we discuss a number of modeling limitations and computational compromises. Ground-motion modeling will improve in reliability in the future as these limitations are overcome, but we believe that the approach used here achieved the goal of providing a more realistic source repre-

sentation than the kinematic parameterization used by Olsen *et al.* (2006).

Resolution of the Numerical Model

While the fault-boundary condition used in our numerical method (stress-glut, Andrews, 1999) has been found to be less accurate than several other implementations (i.e., the boundary integral equations method, BIEM, or the staggered-

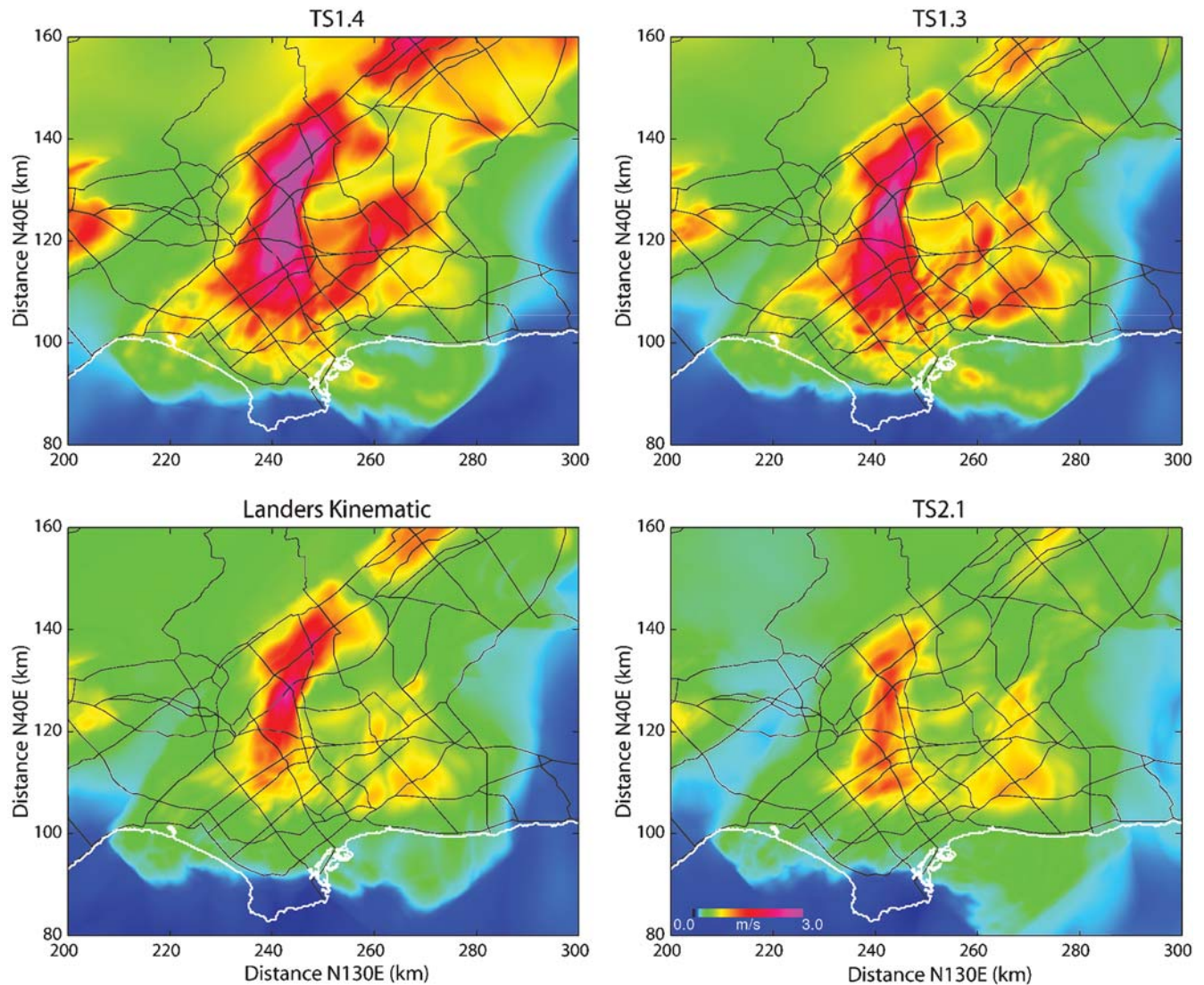


Figure 12. Comparison between PGVs for TS1.4, TS1.3, Landers Kinematic, and TS2.1 inside the black rectangle shown in Figure 1. Lines on the maps depict major freeways and the coastline.

grid split-node (SGSN) method, see Dalguer and Day, 2006, 2007), a simple cohesive-zone analysis shows that our numerical solution is relatively well resolved. For the simple friction model used here, Andrews (1976, 2004) obtained the expression $(C_1/C_2^2)(\mu d_c/\Delta\tau)^2 L^{-1}$ for the length Λ of the cohesive zone (i.e., the portion of the fault plane behind the crack tip where the slip is greater than zero but less than d_c), in which μ is shear modulus, $\Delta\tau$ is dynamic stress drop, L is fault length, and C_1 and C_2 are constants of order one (the analysis is 2D and assumes uniform stress drop). It is this scale length Λ that must be resolved, by several grid cells, in order to achieve numerical accuracy. Day *et al.* (2005) analyzed the cohesive length using a somewhat different approach that yielded the identical result in the limit of large L . In the latter analysis, the divisor involving stress drop and length, which can be written as $(\Delta\tau L^{1/2})^2$, arises from the square of a certain static stress intensity factor, namely, that

associated with the instantaneous slip distribution at the time at which the fault length reaches L . This interpretation guides us in how to apply the Λ estimate in the 3D case with variable stress drop. Because the stress drop enters through its effect on the stress intensity factor (which derives from integrals taken over the fault surface), we estimate a typical value of Λ using the average stress drop in the model, which is 5.4 MPa, and using the fault width (approximately 12 km) for L , because it is that dimension that controls the stress intensity factor for faults that are long compared with their width (e.g., Day, 1982). The resulting estimate, which is supported by direct measurements at different instances of the rupture (see Fig. 14), is that our $dx = 100$ m simulation resolves the cohesive zone with about 14 grid cells (and our $dx = 200$ m simulations have about seven grid cell resolution). Dalguer and Day (2006) estimate that this level of resolution permits rupture to be modeled by the stress-glut

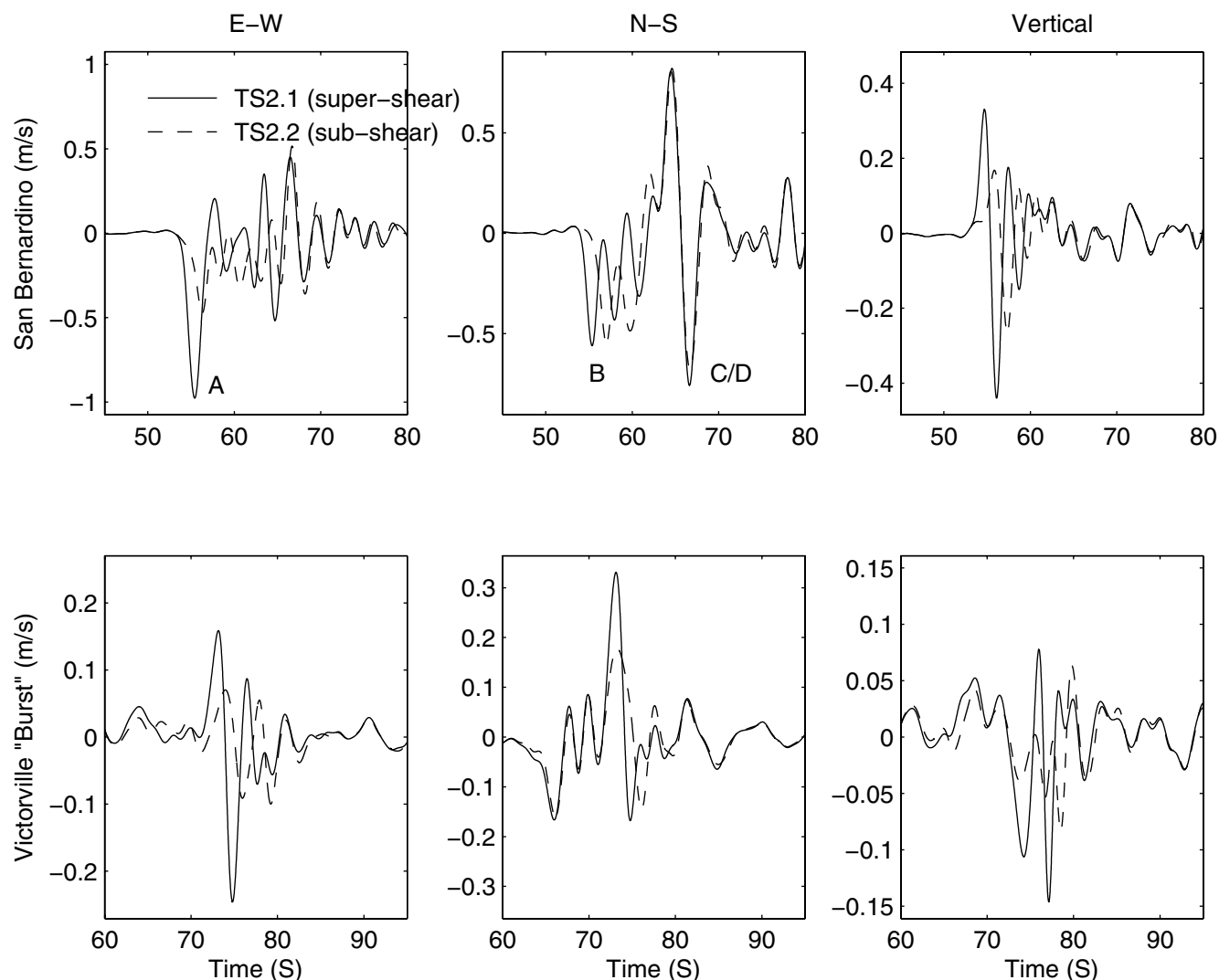


Figure 13. Comparison of synthetic seismograms for TeraShake2.1 and 2.2. (Top) San Bernardino (see Fig. 3 for location). (Bottom) Location inside a band of amplified amplification (burst) northwest of Victorville (see Fig. 7 for location).

method with rupture-velocity errors less than about 3% and peak slip-velocity errors less than about 10%–20%. The worst case would be in the vicinity of the high-stress-drop asperities. Using approximately 8 km for the typical asperity dimension as our estimate of L , and 12 MPa as a rough estimate of the stress drop averaged over the asperity, the local resolution estimate becomes about eight grid cells. In that case, the Dalguer and Day error estimates are only marginally higher than those obtained using averages taken over the entire fault. Thus, the cohesive-zone estimates, with corresponding error estimates from Dalguer and Day (2006), combined with the good agreement between the $dx = 100$ m and $dx = 200$ m simulations, demonstrates that the resolution of these simulations is more than adequate to meet the objectives of the study. Future simulations of this type will be able to achieve considerably higher accuracy (or accommodate significantly more rapid frictional weakening, via a lower d_c or some alternative frictional formulation) through the

use of the SGSN split-node formulation (Dalguer and Day, 2007), for which a parallel implementation has recently become available (Dalguer *et al.*, 2006).

Modeling Procedure

The two-step procedure used in this study, separating the earthquake spontaneous rupture and wave propagation into two different exercises, is a limitation imposed by the choice of numerical method used to simulate rupture and wave propagation. We made this compromise in deference to the extraordinarily large spatial scale of the calculations, which put a premium on the computational efficiencies and high degree of code scalability achieved with the simple Cartesian structured grid used here. However, other numerical methods are capable of simulating the spontaneous rupture and its radiated waves on a nonplanar segmented fault directly in a 3D heterogeneous medium, such as support operator (e.g., Ely *et al.*, 2006) and finite-element (e.g., Anderson *et al.*, 2003;

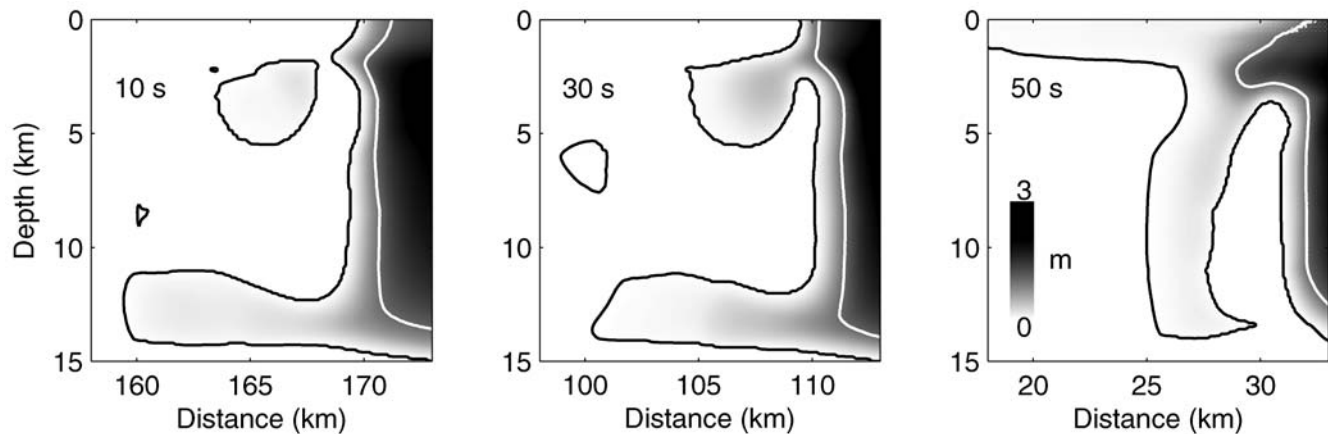


Figure 14. Dynamic slip at three different instances of the TS2.1 rupture (10, 30, and 50 sec after nucleation). The white and black contours depict slip values of 1 mm (approximately equal to the rupture front) and 1 m (equal to d_c). The cohesive zone for the TeraShake2 rupture simulations, estimated as the distance between the two contours, is typically about 1.5 km. This estimate is in agreement with theoretical estimates.

Aagaard *et al.*, 2004; Oglesby *et al.*, 2004) methods. While we believe that the approximations implied in our technique, such as discarding normal stress interaction at fault segment intersections, are relatively minor in the context of our specific objectives in this study, other more flexible numerical methods can be used to refine the modeling in the future. Finally, it is possible that the simplifications involved in the five-segment approximation of the San Andreas fault from Frankel *et al.* (2002) used in our simulations may have affected the ground motions. However, such effects are likely limited, as suggested by strong similarity between the distributions of long-period PGVs in the greater Los Angeles area for TS2 with the ShakeOut scenario on the southern San Andreas fault (Olsen *et al.*, 2007), which used the more detailed fault geometry from the SCEC Community Fault Model (CFM).

Computational Resources

Our modeling of the rupture parameters in the near surface is somewhat arbitrary and meant to generate a limited set of mechanically feasible dynamic rupture propagation models. A more systematic and comprehensive sensitivity study of variations of the parameters is highly desirable but could not be carried out due to computational limitations. Both rupture models and wave propagation runs were carried out on the 10 Teraflops IBM Power4 + DataStar supercomputer at San Diego Supercomputer Center (SDSC) using Message Passing Interface (MPI) to communicate information between individual processors (see Cui *et al.*, 2007 for more information on scaling properties of the code). The high-resolution ($dx = 100$ m) dynamic rupture simulations required 36,000 central processing unit (CPU) hours using 1024 processors, and the wave propagation runs used 14,000 CPU hours on 240 processors. However, while this level of demand for resources limited the number of simulations for our study, the explosive increase in the power of

parallel computers will almost certainly allow for more in-depth analysis of the parameters producing the most physical rupture propagation and thus ground-motion estimates for large hypothetical earthquakes in the near future. Alternatively, the use of dynamic rupture models with nonuniform grids, such as allowed in finite-element or spectral-element approaches, would provide a relatively uniform resolution with respect to the wavelength, with the potential to decrease the required amount of computational resources by an order of magnitude or more for some problems.

Friction Law

The dynamic rupture parameters in the upper part of the fault required special attention in order to avoid unphysically large slip and slip-rate values and to constrain the average rupture speed to a subshear value. We obtained satisfactory results by tapering the initial and normal stress in the upper 2 km of the fault for the entire rupture segment. In addition, we were forced to introduce a weak layer (Day and Ely, 2002) in order to constrain the rupture speed to subshear values in the low-velocity sediments of the San Bernardino area with V_s as low as 500 m/sec. Subshear rupture speeds in the deeper sections of the fault were obtained through a piecewise increase in normal stress in the direction of rupture. As this discussion shows, our treatment of the friction and loading has been based on highly simplified parameterizations, and it is essentially phenomenological. For example, our aim at producing subshear rupture propagation with physical values of slip and slip rate did not require dependency of the normal tractions with depth or a systematic variation of the fault constitutive parameters with shear modulus. We have also not deviated from the elementary friction formulation that has been much employed in the recent past to model ground-motion recordings from large earthquakes. Frictional models are under active development that have a much firmer basis in the mechanics and thermal

physics of rock surfaces in the presence of pore fluids (e.g., Andrews, 2002; Goldsby and Tullis, 2002; DiToro *et al.*, 2004; Bizzarri and Cocco, 2006a,b; Rice, 2006). Once experience has been gained in the successful synthesis of seismic recordings using such models, they should be integrated into future simulations aimed at ground-motion forecasting.

Comparison with Empirical Relations

Empirical attenuation relationships (ARs) attempt to quantify the statistical distribution of ground-motion amplitudes over all scenarios (at a common magnitude, distance, etc.). In this section we compare our specific scenario ground-motion levels for TeraShake2 with an AR in order to rank the scenario ground-motion levels relative to their expected frequency of occurrence for a generic site and event. For this purpose, we will use the AR proposed by Campbell and Bozorgnia (2006 [hereafter, C&B06], 2008), because it includes a depth-dependent basin amplification correction term (adapted from Day *et al.*, 2006, Day, Graves, *et al.*, 2008). Note that for these comparisons we will use the geometric mean of the horizontal-component velocity peaks, because this is the measure of PGV used by C&B06. The geometric mean generates PGVs typically (based on the simulation results) 1.5–2 times smaller than that calculated from the root sum of squares of all three components, the measure used elsewhere in this study.

First we compare PGV values for TS2.1–2.3 and C&B06 at three million rock sites (see Fig. 15) at distances up to 200 km from the fault. The rock sites (70% of the model area) were defined by a surface $V_s > 1000$ m/sec for TS2 (the SCEC CVM does not include a weathered layer for rock sites, which would reduce these surficial V_s values by a factor of 2 to 3 without significantly affecting ground motion in the 0–0.5-Hz band) and a depth of 400 m to the $V_s = 2500$ m/sec isosurface for C&B06 (and $V_s30 = 760$ m/sec). For most distances from the fault, the median TS2 and C&B06 PGVs agree very well for all three scenarios. The maximum TS2 PGVs at rock sites are less than the C&B06 2% POE level for almost all distances included here. The minimum TS2 PGVs at rock sites are generally between the C&B06 98% and 99.9% POE levels for the southeast–northwest rupture scenarios (TS2.1–2.2), but up to a factor 2 lower than the 99.9% POE level for the northwest–southeast rupture scenario (TS2.3). The agreement provides independent evidence that the fault area (and therefore the average stress drop) adopted for the TS2 scenarios is consistent with a moment magnitude of 7.7. The absence of highly improbable extremes in the rock-site PGVs supports our treatment of the shallow 2 km of the fault as a mechanically weak zone with little or no dynamic stress drop.

Table 4 compiles PGV values from TS2.1–2.3 for some selected sediment sites and shows, for comparison, the predicted C&B06 AR distributions at POE levels (50% [the median], 16%, 2%, and 0.13%) for six selected sites (L1–L6 in Fig. 16). PGVs for the complementary higher-than-median

POE levels (i.e., 84%, 98%, and 99.87% POE) are not shown, but their ratios to the median ground motion are inverse to those given. The selected sites in Table 4 fall into three categories. (1) Near fault: locations L1 and L2 are both at 1 km from the rupture trace, selected for being, respectively, the sites of the largest and smallest TS2.1 PGVs at that distance. (2) Wave-guide dominated: location L3 is the site of the maximum PGV for TS2.1 in the high-amplitude sedimentary channel mentioned previously. (3) Los Angeles basin: Location L4 is in the center of downtown Los Angeles, and L5 and L6 are sites of the maximum and minimum TS2.1 PGVs, respectively, within the deepest part of the Los Angeles basin (defined by depths greater than about 5 km to the 2.5 km/sec *S*-wave velocity isosurface). We make the following observations:

1. Near-fault PGVs from the simulations are similar to expectations based on the AR. The largest near-fault PGVs (about 220 cm/sec, at sites like L1, at about 1 km from the fault and on deep sediments in the Salton Trough) are comparable to or slightly larger than the largest observed PGVs from historical earthquakes (typically 1–2 m/sec, e.g., 1994 M_w 6.7 Northridge, 1992 M_w 7.3 Landers, 1999 M_w 7.6 Chi-Chi, and 2002 M_w 7.9 Denali events). Moreover, these maxima are only about a factor of 2 above the C&B06 median. That is, the upper extremes of the AR distribution (which result if an untruncated log-normal distribution is assumed) are not present at near-fault sites in the simulations. On the other hand, the lower extremes predicted by the AR distribution are represented in the simulations. For example, the minimum near-fault PGV of 17 cm/sec from TS2.1, at L2, is somewhat below the 99.9% POE level.
2. The highly localized maximum in PGV associated with focusing in the sedimentary channel (L3, at Whittier–Narrows near the junction between Los Angeles and San Gabriel basins) is at roughly the 0.1%–0.2% POE level of the AR for the worst-case directivity simulations (TS2.1 and TS2.2). Furthermore, it remains high (at the about 16% POE level) even for the backward directivity case (TS2.3).
3. The deeper parts of the Los Angeles basin (L5, L6) have ground motion everywhere anomalously high relative to AR-based expectations—ranging between the 16% and 0.13% POE levels in the forward-directivity scenarios, and near the median AR value in the backward directivity case. The AR estimates already include a correction term for amplification due to local basin depth beneath a site. Thus, the anomalous amplitudes appear to reflect the important nonlocal effects revealed by the simulations: the channeling of energy into the deep parts of the basin by the sedimentary waveguides and perhaps also the convergence of guided waves from two distinct sedimentary paths. At the downtown site (L4), on shallower sediments and away from the principal zone influenced by the convergent guided waves, PGVs are quite close to the AR

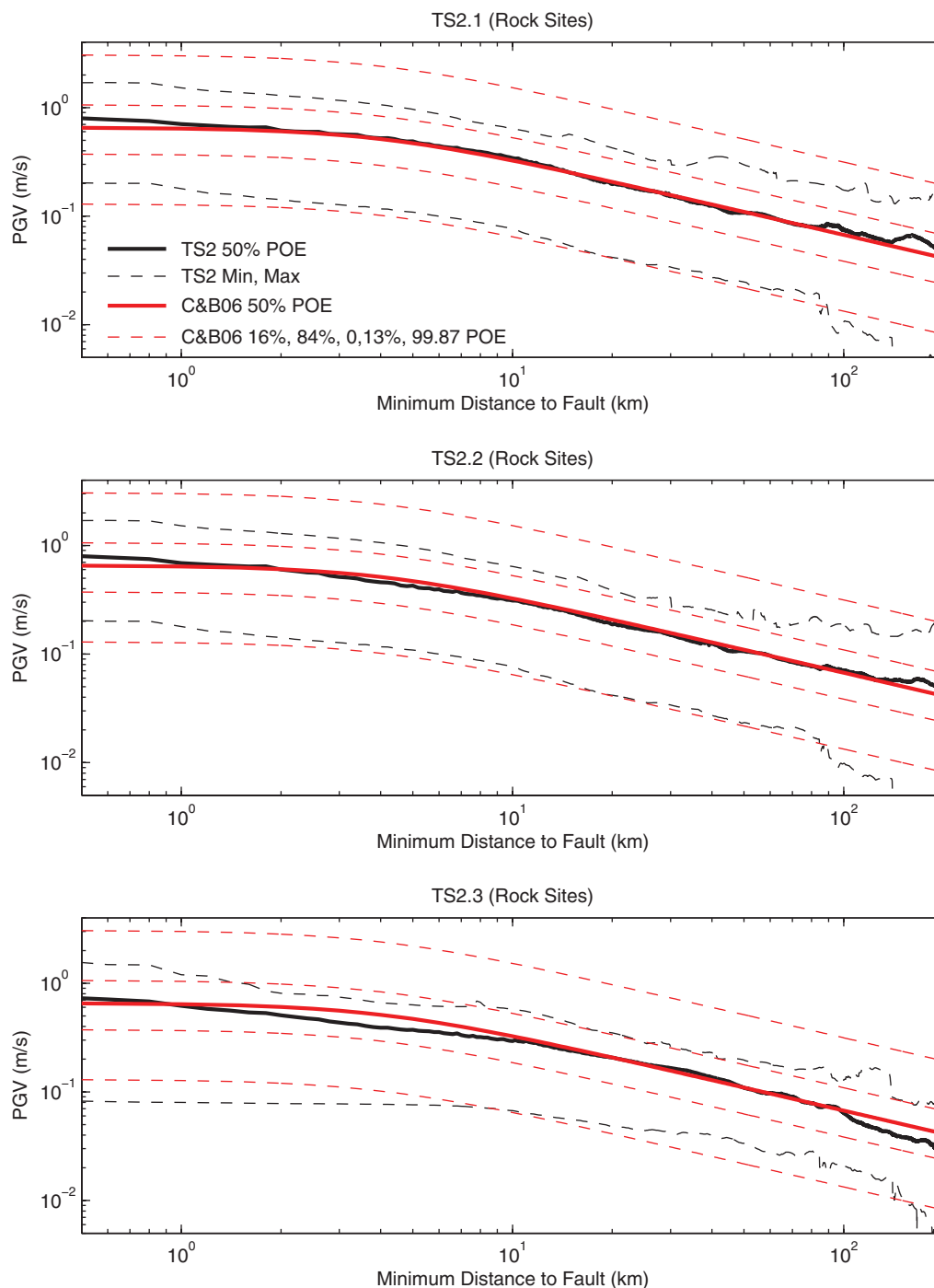


Figure 15. Comparison of PGVs from TS2.1–2.3 to those calculated for a M_w 7.7 from C&B06 from rock sites. The rock sites were defined by a surface $V_s > 1000$ m/sec for TS2 and a depth of 400 m to the $V_s = 2500$ m/sec isosurface for C&B06 (and $V_{s30} = 760$ m/sec).

prediction (ranging over roughly a factor of 2 above and below the median C&B06 prediction).

Discussion and Conclusions

We have used spontaneous rupture models, with stress-drop heterogeneity based on inferences from the 1992 Land-

ers earthquake (TeraShake2), to estimate ground motions from M_w 7.7 earthquakes on the southern San Andreas fault, and we compared the results with those generated by sources based on the kinematic parameterizations of the 2002 Denali event (TeraShake1, Olsen *et al.*, 2006). The TeraShake2 models have average slip, rupture velocity, and slip duration that are nearly the same as the corresponding values for the

Table 4
PGVs for TS2 Versus C&B06 at Selected Sites

Site	Description	PGV, TS2 (cm/sec)			PGV, C&B06 AR (cm/sec)			
		2.1	2.2	2.3	Median	16% POE	2% POE	0.13% POE
L1	Near-fault maximum $D = 3.9$ km, $R_{rup} = 1$ km	219	227	116	122	206	356	593
L2	Near-fault minimum $D = 3.9$ km, $R_{rup} = 1$ km	17	17	48	122	206	356	593
L3	Wave-guide maximum $D = 4.1$ km, $R_{rup} = 61$ km	104	105	36	20	33	58	95
L4	Los Angeles downtown $D = 2.8$ km, $R_{rup} = 75$ km	28	27	6.9	13	22	39	65
L5	Deep basin maximum $D = 5.9$ km, $R_{rup} = 78$ km	97	93	25	23	39	68	112
L6	Deep basin minimum $D = 5.3$ km, $R_{rup} = 74$ km	46	77	27	23	38	66	109

Selection criteria for L1–L3 and L5 and L6 based on PGVs for TS2.1.

Sediment thickness (D) defined by the $V_s = 2.5$ km/sec isosurface from the SCEC CVM3.0.

R_{rup} is closest distance to the fault.

Nominal $V_{s,30}$ (upper 30-m average V_s of 360 m/sec assumed for C&B06 site term at L1, L2, and L3).

$V_{s,30}$ values from SCEC CVM3.0 were used at L4, L5, and L6 (374, 302, and 297 m/sec, respectively).

Sites L5 and L6 (see Fig. 15) are selected visually for locations in the main Los Angeles basin with depths to the $V_s = 2.5$ km/sec isosurface larger than about 5 km.

TeraShake1 sources, and yet the ground-motion predictions for the two source types are significantly different. In particular, the increased complexity of the TeraShake2 sources decreases the largest peak ground motions associated with the wave guides and deep basin amplification by factors of 2–3, as compared to those from the TeraShake1 simulations. This reduction of ground-motion extremes results largely from the less coherent wave field radiated by the TeraShake2 sources. The corresponding constant-rupture-velocity simulation (Landers kinematic) shows that this reduction is primarily a consequence of spontaneously occurring fluctuations in the speed, shape, and propagation di-

rection of the slip pulse. This result is consistent with the interpretation by Day, Gonzalez, *et al.* (2008) of laboratory scale-model earthquakes. They showed that the experiments substantially overpredict rupture-induced forward directivity of near-fault motions, in comparison with empirical data from natural earthquakes, and they attributed the difference in part to incoherence of rupture in the latter.

Rupture complexity of this type may prove quite difficult to parameterize effectively in a purely kinematic source description. Nevertheless, because these source complexities appear to have a potentially large effect on simulation-based ground-motion estimates, they should be incorporated into

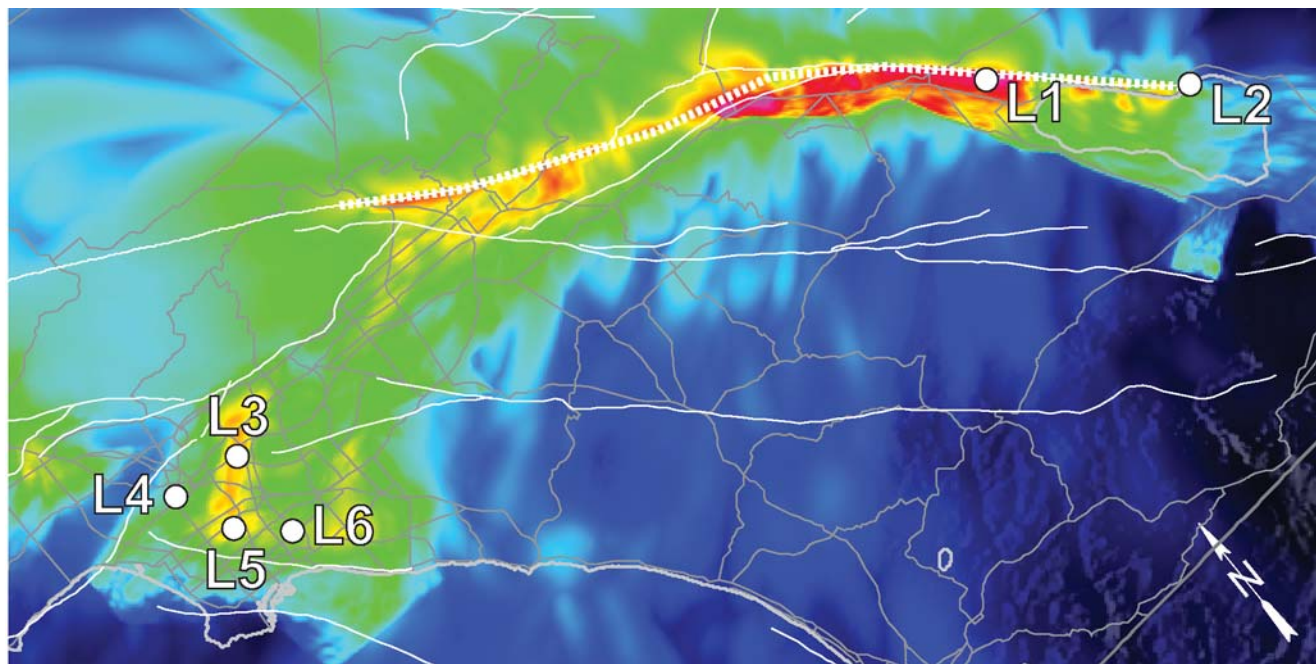


Figure 16. Close-up of the PGVs for the TeraShake2.1 simulation from Figure 7 (top), showing the sites L1–L6 where TS2 PGVs are compared to those from C&B06. White lines depict fault traces, and gray lines depict major freeways, the coastline, and political boundaries. The dotted line depicts the part of the San Andreas fault that ruptured in the TeraShake2 simulations.

kinematic models designed to emulate spontaneous rupture. An example of such efforts are the pseudodynamic source descriptions proposed by Guatteri *et al.* (2004), where rupture parameters, such as rupture initiation and rise time, as well as the shape of the slip history, are dependent on a spatially variable slip distribution and hypocenter location. While this method generates rupture models much superior to earlier, strongly simplified rupture models, the differences between the TeraShake1 and TeraShake2 simulations suggest that further improvement of the source description may be needed. For example, the pseudodynamic method, as it is currently implemented, does not produce ruptures with abrupt changes in rupture directions, which removed energy from the forward-directivity cone and generated the characteristic burst patterns of elevated peak ground motions in the TeraShake2 results.

Despite these differences in amplitude extremes, there is considerable similarity between the spatial patterns of ground-motion excitation for the TeraShake1 and TeraShake2 scenarios with a common rupture direction. For example, the band of amplification extending from the San Gabriel basin through Whittier–Narrows into the Los Angeles basin, for the southeast–northwest rupture scenarios TS2.1–2.2 (see Fig. 7), is similar to the pattern found in the TeraShake1 southeast–northwest simulations (Olsen *et al.*, 2006). Moreover, a second wave guide, although less effective in channeling the surface waves, generates the multipathing effect discussed earlier and causes increased amplification in the southern part of the Los Angeles basin (see Fig. 8) for both sets of TeraShake simulations. Thus, the TeraShake1 and TeraShake2 results indicate that such sedimentary wave-guide effects, where they exist, may have a large systematic impact on long-period shaking levels. A caveat to this conclusion is that the same 3D velocity model (SCEC CVM 3.0) was used for all TeraShake calculations, and the details of the amplification pattern may be sensitive to uncertainties in this structure. Future simulations will examine the sensitivity of these important effects to uncertainties in geologic structure through the use of alternative 3D models (e.g., Süß and Shaw, 2003), and the uncertainties will be reduced as new models become available that incorporate tomographic refinements of the SCEC CVM (Chen *et al.*, 2007).

An important conclusion of our study is that much of the variability in long-period ground motion that is subsumed into uncertainty estimates of the current empirical ARs can be modeled and understood deterministically through numerical simulations with results that have significant implications for earthquake hazard assessment. In the three TeraShake2 simulations, we see large systematic amplification effects, both from scenario-specific rupture directivity and region-specific geologic structures. Naturally, these complex source propagation, wave-guide, and 3D basin amplification effects, which are of first-order importance in scenario ground-motion estimates, cannot be captured by ARs estimated from many earthquakes with a large variation of source, path, and

site effects (and with limited observational constraint at large magnitude). In particular, the very localized extremes in PGV predicted near Whittier–Narrows, due to focusing of channeled waves, are up to a factor of 5 above the median prediction of the current generation of ARs. The same channeling effect leads to pervasive amplifications in the deep parts of Los Angeles basin that are a factor of 2–4 above the median AR (even when, as in the C&B06 AR, a correction for local basin depth is included). Although we have modeled these effects for a specific set of scenarios, they are sufficiently strong for some sites to influence predictions from ensemble averages of sources, and therefore should be considered in probabilistic seismic hazard analysis (PSHA). An effort to include physics-based 3D ground-motion simulations in PSHA is underway in the SCEC CyberShake project (Deelman *et al.*, 2006), which can be expected to significantly improve the accuracy of hazard estimation in southern California.

The ground-motion estimates in this study are for M_w 7.7 earthquakes on the southern San Andreas fault. This magnitude is based on an average slip rate of 16 mm/yr, leading to an average slip deficit of about 5 m since the last large event on the southern San Andreas fault. Based upon our current understanding, an earthquake of this magnitude is certainly possible for that segment of the San Andreas fault (Frankel *et al.*, 2002). The rock-site comparisons with the Next Generation Attenuation relationships for median PGV suggest that M_w 7.7 is a fairly representative magnitude for the given fault area, though the attenuation relationships themselves have rather minimal observational constraint at this value of M_w . Earthquakes rupturing a similar fault area, but with lower average slip (and therefore lower average stress drop), are also plausible, and such events would generate peak ground motions in our simulations that are smaller, roughly in proportion to total slip. For example, compared to a M_w 7.7 event, peak motions for a M_w 7.5 (moment of 2×10^{20} N m) earthquake with comparable directivity and basin effects are reduced by approximately a factor of 2.

Acknowledgments

We thank reviewers Eric Dunham and Brad Aagaard for very helpful comments. The TeraShake2 project is funded by National Science Foundation (NSF) ITR through Award Number EAR-0122464 (The SCEC Community Modeling Environment [SCEC/CME]: an Information Infrastructure for System-Level Earthquake Research). SCEC is funded through the NSF Cooperative Agreement Number EAR-0106924 and USGS Cooperative Agreement Number 02HQAG0008. SDSC's computational effort was supported through the NSF-funded SDSC Strategic Applications Collaborations (SAC) and Strategic Community Collaborations (SCC) programs. The large-scale computation, storage, visualization, and access to scientific programming were made possible by awards from the TeraGrid (TG-MCA03S012). The synthetic seismograms from TeraShake2 are available online at the Storage Resource Broker (SRB) at SDSC. This is SCEC Contribution Number 1148.

References

- Aagaard, B. T., G. Anderson, and K. W. Hudnut (2004). Dynamic rupture modeling of the transition from thrust to strike-slip motion in the 2002 Denali fault, Alaska, earthquake, *Bull. Seismol. Soc. Am.* **94**, S190–S201.
- Anderson, G., B. Aagaard, and K. Hudnut (2003). Fault interactions and large complex earthquakes in the Los Angeles area, *Science* **302**, no. 5652, 1946–1949.
- Andrews, D. J. (1976). Rupture propagation with finite stress in antiplane strain, *J. Geophys. Res.* **81**, 3575–3582.
- Andrews, D. J. (1999). Test of two methods for faulting in finite-difference calculations, *Bull. Seismol. Soc. Am.* **89**, 931–937.
- Andrews, D. J. (2002). A fault constitutive relation accounting for thermal pressurization of pore fluid, *J. Geophys. Res.* **107**, 2363 doi 10.1029/2002JB001942.
- Andrews, D. J. (2004). Rupture models with dynamically-determined breakdown displacement, *Bull. Seismol. Soc. Am.* **94**, 769–775.
- Archuleta, R. J. (1984). A faulting model for the 1979 Imperial Valley earthquake, *J. Geophys. Res.* **89**, 4559–4585.
- Bizzarri, A., and M. Cocco (2006a). A thermal pressurization model for the spontaneous dynamic rupture propagation on a three-dimensional fault: 1. Methodological approach, *J. Geophys. Res.* **111**, B05303, doi 10.1029/2005JB003862.
- Bizzarri, A., and M. Cocco (2006b). A thermal pressurization model for the spontaneous dynamic rupture propagation on a three-dimensional fault: 2. Traction evolution and dynamic parameters, *J. Geophys. Res.* **111**, B05304, doi 10.1029/2005JB003864.
- Bouchon, M., M. P. Bouin, H. Karabulut, M. N. Toksöz, M. Dietrich, and A. Rosakis (2001). How fast is rupture during an earthquake? New insights from the 1999 Turkey earthquakes, *Geophys. Res. Lett.* **28**, 2723–2726.
- Brune, J., and R. Anooshehpour (1998). A physical model of the effect of a shallow weak layer on strong ground motion for strike-slip ruptures, *Bull. Seismol. Soc. Am.* **88**, 1070–1078.
- Campbell, K. W., and Y. Bozorgnia (2006). Pacific Earthquake Engineering Research (PEER) Report, Campbell-Bozorgnia NGA empirical ground motion model for the average horizontal component of PGA, PGV, PGD and SA at selected spectral periods ranging from 0.01–10.0 seconds, http://peer.berkeley.edu/products/rep_nga_models.html (last accessed May 2008).
- Campbell, K. W., and Y. Bozorgnia (2008). Campbell-Bozorgnia NGA horizontal ground motion model for PGA, PGV, PGD and 5% damped linear elastic response spectra for periods ranging from 0.01 to 10 s, *Earthq. Spectra* (in press).
- Chen, P., L. Zhao, and T. H. Jordan (2007). Full 3D tomography for crustal structure of the Los Angeles region, *Bull. Seismol. Soc. Am.* **97**, no. 4, 1094–1120, doi 10.1785/0120060222.
- Chourasia, A., S. Cutchin, Yifeng Cui, R. W. Moore, K. Olsen, S. M. Day, J. B. Minster, P. Maechling, and T. H. Jordan (2007). Visual insights into high-resolution earthquake simulations, *Comput. Graph. Appl. J.* **27**, no. 5, 28–34.
- Cruz-Atienza, V. M., J. Virieux, and H. Aochi (2007). 3D finite-difference dynamic-rupture modeling along nonplanar faults, *Geophysics* **72**, SM123–SM137.
- Cui, Y., R. Moore, K. Olsen, A. Chourasia, P. Maechling, B. Minster, S. Day, Y. Hu, J. Zhu, A. Majumdar, and T. Jordan (2007). Enabling very-large scale earthquake simulations on parallel machines. Advancing science and society through computation, in *International Conference on Computational Science 2007, Part I*, Lecture Notes in Computer Science, Vol. **4487**, Springer, New York, 46–53.
- Dalguer, L. A., and S. M. Day (2006). Comparison of fault representation methods in finite difference simulations of dynamic rupture, *Bull. Seismol. Soc. Am.* **96**, 1764–1778.
- Dalguer, L. A., and S. M. Day (2007). Staggered-grid split-node method for spontaneous rupture simulation, *J. Geophys. Res.* **112**, B02302, doi 10.1029/2006JB004467.
- Dalguer, L. A., S. M. Day, K. B. Olsen, and Y. Cui (2006). Implementation of the staggered-grid split-node method in a MPI finite difference code for large scale models of spontaneous dynamic rupture simulations, in *SCEC Annual Meeting*, Palm Springs, 9–14 September.
- Day, S. M. (1982). Three-dimensional finite difference simulation of fault dynamics: rectangular faults with fixed rupture velocity, *Bull. Seismol. Soc. Am.* **72**, 705–727.
- Day, S. M., and C. Bradley (2001). Memory-efficient simulation of anelastic wave propagation, *Bull. Seismol. Soc. Am.* **91**, 520–531.
- Day, S. M., and G. Ely (2002). Effect of a shallow weak zone on fault rupture: numerical simulation of scale-model experiments, *Bull. Seismol. Soc. Am.* **92**, S214–S233.
- Day, S. M., J. Bielak, D. Dreger, R. Graves, S. Larsen, K. B. Olsen, A. Pitarka, and L. Ramirez-Guzman (2006). Numerical simulation of basin effects on long-period ground motion, in *Proceedings of the Eighth National Conference on Earthquake Engineering*, San Francisco, California.
- Day, S. M., L. A. Dalguer, N. Lapusta, and Y. Liu (2005). Comparison of finite difference and boundary integral solutions to three-dimensional spontaneous rupture, *J. Geophys. Res.* **110**, B12307, doi 10.1029/2005JB003813.
- Day, S. M., S. H. Gonzalez, R. Anooshehpour, and J. N. Brune (2008). Scale-model and numerical simulations of near-fault seismic directivity, *Bull. Seismol. Soc. Am.* **98**, 1186–1206.
- Day, S. M., R. W. Graves, J. Bielak, D. Dreger, S. Larsen, K. B. Olsen, A. Pitarka, and L. Ramirez-Guzman (2008). Model for basin effects on long-period response in southern California, *Earthq. Spectra* (in press).
- Deelman, E., G. Mehta, R. Graves, L. Zhao, N. Gupta, P. Maechling, and T. Jordan (2006). Managing large-scale workflow execution from resource provisioning to provenance tracking: the CyberShake example, in *IEEE e-Science and Grid Computing 2006*, Amsterdam, Netherlands, December 2006.
- DiToro, G., D. L. Goldsby, and T. E. Tullis (2004). Friction falls towards zero in quartz rock as slip velocity approaches seismic rates, *Nature* **47**, 436–439.
- Dunham, E. M., and R. J. Archuleta (2005). Near-source ground motion from steady state dynamic rupture pulses, *Geophys. Res. Lett.* **32**, L03302, doi 10.1029/2004GL021793.
- Ely, G. P., J. B. Minster, and S. M. Day (2006). Large scale dynamic rupture modeling with realistic geometry (Abstract S41C-1350) *EOS Trans. AGU* **87**, no. 52 (Fall Meet. Suppl.), S41C-1350.
- Frankel, A. D., M. D. Petersen, C. S. Muller, K. M. Haller, R. L. Wheeler, E. V. Leyendecker, R. L. Wesson, S. C. Harmsen, C. H. Cramer, D. M. Perkins, and K. S. Rukstales (2002). Documentation for the 2002 update of the National Seismic Hazard Maps, *U.S. Geol. Surv., Open-File Rept.* **02-420**, 33 p.
- Goldsby, D. L., and T. E. Tullis (2002). Low frictional strength of quartz rocks at subseismic slip rates, *Geophys. Res. Lett.* **29**, no. 17, 1844.
- Gottschämmer, E., and K. B. Olsen (2001). Accuracy of the explicit planar free-surface boundary condition implemented in a fourth-order staggered-grid velocity-stress finite-difference scheme, *Bull. Seismol. Soc. Am.* **91**, 617–623.
- Graves, R. W. (1998). Three-dimensional finite-difference modeling of the San Andreas fault: source parameterization and ground-motion levels, *Bull. Seismol. Soc. Am.* **88**, 881–897.
- Guatteri, M., P. M. Mai, and G. C. Beroza (2004). A pseudo-dynamic approximation to dynamic rupture models for strong ground motion prediction, *Bull. Seismol. Soc. Am.* **94**, no. 6, 2051–2063.
- Ide, S. I. (2002). Estimation of radiated energy of finite-source earthquake models, *Bull. Seismol. Soc. Am.* **92**, 2994–3005.
- Krishnan, S., C. Ji, D. Komatitsch, and J. Tromp (2006a). Case studies of damage to tall steel moment-frame buildings in southern California during large San Andreas earthquakes, *Bull. Seismol. Soc. Am.* **96**, no. 4, 1523–1537.
- Krishnan, S., C. Ji, D. Komatitsch, and J. Tromp (2006b). Performance of two 18-story steel moment-frame buildings in southern California dur-

- ing two large simulated San Andreas earthquakes, *Earthq. Spectra* **22**, no. 4, 1035–1061.
- Magistrale, H., S. Day, R. Clayton, and R. Graves (2000). The SCEC southern California reference three-dimensional seismic velocity model version 2, *Bull. Seismol. Soc. Am.* **90**, S65–S76.
- Marcinkovich, C., and K. B. Olsen (2003). On the implementation of perfectly matched layers in a 3D fourth-order velocity-stress finite-difference scheme, *J. Geophys. Res.* **108**, no. B5, 2276, doi 10.1029/2002JB002235.
- Marone, C., and C. H. Scholz (1988). The depth of seismic faulting and the upper transition from stable to unstable slip regimes, *Geophys. Res. Lett.* **15**, 621–624.
- Nielsen, S. B., and K. B. Olsen (2000). Constraints on stress and friction from dynamic rupture models of the 1994 Northridge, California, earthquake, *Pure Appl. Geophys.* **157**, 2029–2046.
- Oglesby, D. D., D. S. Dreger, R. A. Harris, N. Ratchkovski, and R. Hansen (2004). Inverse kinematic and forward dynamic models of the 2002 Denali, Alaska earthquake, *Bull. Seismol. Soc. Am.* **94**, no. B6, S214–S233.
- Olsen, K. B. (1994). Simulation of three-dimensional wave propagation in the Salt Lake basin, *Ph.D. Thesis*, University of Utah, Salt Lake City, Utah, 157 p.
- Olsen, K. B., R. J. Archuleta, and J. R. Matarese (1995). Three-dimensional simulation of a magnitude 7.75 earthquake on the San Andreas fault in southern California, *Science* **270**, 1628–1632.
- Olsen, K. B., S. M. Day, and C. R. Bradley (2003). Estimation of Q for long-period (> 2 s) waves in the Los Angeles basin, *Bull. Seismol. Soc. Am.* **93**, 627–638.
- Olsen, K. B., S. M. Day, Y. Cui, J. Zhu, G. Juve, and P. Maechling (2007). ShakeOut: 1 Hz ground motion simulations for the southern San Andreas fault, *Proc. SCEC Annual Meeting*, Palm Springs, 153 pp.
- Olsen, K. B., S. M. Day, J. B. Minster, Y. Cui, A. Chourasia, M. Faerman, R. Moore, P. Maechling, and T. Jordan (2006). Strong shaking in Los Angeles expected from southern San Andreas earthquake, *Geophys. Res. Lett.* **33**, L07305, doi 10.1029/2005GL025472.
- Peyrat, S., K. B. Olsen, and R. Madariaga (2001). Dynamic modeling of the 1992 Landers earthquake, *J. Geophys. Res.* **106**, 26,467–26,482.
- Rice, J. R. (2006). Heating and weakening of faults during earthquake slip, *J. Geophys. Res.* **111**, B05311, doi 10.1029/2005JB004006.
- Stiess, M. P., and J. H. Shaw (2003). P -wave seismic velocity structure derived from sonic logs and industry reflection data in the Los Angeles basin, California, *J. Geophys. Res.* **108**, no. B3, 2170.
- Tinti, E., P. Spudich, and M. Cocco (2005). Earthquake fracture energy inferred from kinematic rupture models on extended faults, *J. Geophys. Res.* **110**, B12303, doi 10.1029/2005JB003644.
- Xia, K., A. J. Rosakis, and H. Kanamori (2004). Laboratory earthquakes: the sub-Rayleigh-to-supershear rupture transition, *Science* **303**, 1859–1861.
- Weldon, R., K. Scharer, T. Fumal, and G. Biasi (2004). Wrightwood and the earthquake cycle: what a long recurrence record tells us about how faults work, *GSA Today* **14**, 4–10.
- Working Group on California Earthquake Probabilities (1995). Seismic hazards in southern California: probable earthquake, 1994 to 2024, *Bull. Seismol. Soc. Am.* **85**, 379–439.

Department of Geological Sciences
San Diego State University
San Diego, California 92182
(K.B.O., S.M.D.)

Scripps Institution of Oceanography
La Jolla, California 92093
(J.B.M.)

San Diego Supercomputer Center
La Jolla, California 92093
(Y.C., A.C.)

University of Southern California
Los Angeles, California 90089
(D.O., P.M., T.J.)

Manuscript received 12 June 2007